

HIGHER ORDER DISCONTINUOUS FINITE ELEMENT METHODS FOR
DISCRETE ORDINATES THERMAL RADIATIVE TRANSFER

A Dissertation

by

PETER GREGORY MAGINOT

Submitted to the Office of Graduate and Professional Studies of
Texas A&M University
in partial fulfillment of the requirements for the degree of

DOCTOR OF PHILOSOPHY

Co-Chairs of Committee,	Jim E. Morel
	Jean C. Ragusa
Committee Members,	Marvin L. Adams
	Jean-Luc Guermond
Head of Department,	Yassin A. Hassan

May 2015

Major Subject: Nuclear Engineering Department

Copyright 2015 Peter Gregory Maginot

ABSTRACT

Lorem ipsum dolor sit amet, consectetur adipiscing elit. Integer lectus quam, condimentum quis bibendum eu, sollicitudin eget lacus. Praesent non sodales odio. Class aptent taciti sociosqu ad litora torquent per conubia nostra, per inceptos himenaeos. Nulla ac luctus sapien. Morbi cursus sapien eget lorem fermentum hendrerit. Nam ac erat dui, in cursus velit. Vivamus hendrerit porttitor nisi, ut porttitor lorem volutpat eget. In ligula ligula, euismod ut condimentum sit amet, pulvinar sit amet diam. Pellentesque interdum, ipsum ullamcorper consequat dignissim, sem arcu egestas mauris, vitae interdum sem tortor ut ante. Nunc blandit laoreet nisi, non rutrum lorem hendrerit quis. Cras nunc diam, convallis et feugiat at, auctor id libero. Nunc facilisis massa eu eros imperdiet vestibulum. Vestibulum ante ipsum primis in faucibus orci luctus et ultrices posuere cubilia Curae; Donec non velit vitae tortor blandit semper.

Etiam vitae dolor nulla. Ut eros odio, rhoncus eget placerat vitae, elementum ac ante. Proin vitae odio eu nisl pharetra mattis. Pellentesque habitant morbi tristique senectus et netus et malesuada fames ac turpis egestas. Phasellus fermentum lacus consectetur neque consequat ullamcorper. Cras blandit urna non dui consequat molestie. Curabitur viverra nibh at nisi semper faucibus. Nam egestas mauris a enim dignissim nec consectetur tortor rutrum. Mauris at nisi in est luctus congue ut mattis est. Ut pretium, mi quis elementum cursus, ante eros suscipit ligula, ut porttitor elit leo sed turpis. Nam sed dui ligula.

DEDICATION

To my wife, Kelli, for traveling with me along all the unforeseen curves of life.
To my mom and dad, for providing my foundation and inspiration.

ACKNOWLEDGEMENTS

I am thankful for the years of teaching and guidance provided by my co-chairs Dr. Jean Ragusa and Dr. Jim Morel; you convinced me long ago that a career in research was worth the extra challenges, costs, and years of work. I would also like to thank Dr. Marvin Adams for initially guiding me to the Computational Methods Group at Texas A&M and for encouraging me to consider Lawrence Livermore National Laboratory for post-graduation employment. Additionally, I thank I would like to thank Dr. Jean-Luc Guermond for your time and feedback on this dissertation and the master's thesis that preceeded it. Finally, I wish to thank the Department of Energy Computational Science Graduate Fellowship (administered by the Krell institute under grant number DE-FG02-97ER25308) for financial support during this work.

NOMENCLATURE

B/CS	Bryan/College Station
HSUS	Humane Society of the United States
P	Pressure
T	Time
TVA	Tennessee Valley Authority
TxDOT	Texas Department of Transportation

This page is optional.

TABLE OF CONTENTS

	Page
ABSTRACT	ii
DEDICATION	iii
ACKNOWLEDGEMENTS	iv
NOMENCLATURE	v
TABLE OF CONTENTS	vi
LIST OF FIGURES	viii
LIST OF TABLES	xi
1. INTRODUCTION	1
1.1 Simplifications of the Thermal Radiative Transfer Equations	2
1.2 Spatial and Temporal Discretization	3
1.2.1 Time Integration	3
1.2.2 Spatial Discretization with Discontinuous Finite Elements	3
1.3 Progression Towards Higher Order DFEM Thermal Radiative Transfer	4
2. DISCONTINUOUS FINITE ELEMENTS FOR RADIATION TRANSPORT	6
2.1 History of DFEM for Neutron Transport	6
2.2 Matrix Lumping Techniques to Study	8
2.3 Lumping Techniques for the 1-D S_N Neutron Transport Equation with Arbitrary Order DFEM	10
2.3.1 Weak Form Derivation	10
2.3.2 Traditional Lumping	15
2.3.3 Quadrature-Based Lumping	15
2.3.4 Source Moment Evaluation	15
2.4 Quadrature Point Selection	16
2.5 Numerical Results	20
2.5.1 Incident Flux Single-Cell Outflow Comparison	21
2.5.2 Fixed Source Single-Cell Inflow Comparison	23
2.5.3 Single-Cell Taylor Series Analysis	27

2.5.4	Convergence Rates for Spatially Discretized 1-D Domains . . .	35
3.	LAST CHAPTER: THE IMPORTANCE OF RESEARCH	49
3.1	New Section	49
3.2	Another Section	49
3.2.1	Subsection	50
3.2.2	Subsection	50
3.3	Another Section	50
4.	LAST CHAPTER: THE IMPORTANCE OF RESEARCH	52
4.1	New Section	52
5.	LAST CHAPTER: THE IMPORTANCE OF RESEARCH	53
5.1	New Section	53
6.	LAST CHAPTER: THE IMPORTANCE OF RESEARCH	54
6.1	New Section	54
	REFERENCES	56
	APPENDIX A. FIRST APPENDIX	60
	APPENDIX B. SECOND APPENDIX WITH A LONGER TITLE - MUCH LONGER IN FACT	62
	B.1 Appendix Section	62

LIST OF FIGURES

FIGURE	Page
2.1 Numerical outflow values as a function of h , for a single cell homogeneous absorber problem with a linear DFEM trial space.	22
2.2 Numerical outflow values as a function of h , for a single cell homogeneous absorber problem with a quadratic DFEM trial space.	23
2.3 Numerical outflow values as a function of h , for a single cell homogeneous absorber problem with a cubic DFEM trial space.	24
2.4 Numerical outflow values as a function of h , for a single cell homogeneous absorber problem with a quartic DFEM trial space.	25
2.5 Numerical inflow values as a function of $\frac{S_1}{S_0}$ for a single cell (vacuum case) with a δ -shaped source, using polynomial orders $P = 1$ through $P = 4$	26
2.6 Numerical inflow values as a function of $\frac{S_1}{S_0}$ for a single cell (vacuum case) with a δ -shaped source, using polynomial orders $P = 1$ through $P = 4$	27
2.7 Numerical inflow values as a function of $\frac{S_1}{S_0}$ for a single cell (vacuum case) with a δ -shaped source, using polynomial orders $P = 1$ through $P = 4$	28
2.8 Numerical inflow values as a function of $\frac{S_1}{S_0}$ for a single cell (vacuum case) with a δ -shaped source, using polynomial orders $P = 1$ through $P = 4$	29
2.9 Numerical inflow values as a function of $\frac{S_1}{S_0}$, for a single cell (absorber case) with a δ -shaped source, using polynomial orders $P = 1$ through $P = 4$	30
2.10 Numerical inflow values as a function of $\frac{S_1}{S_0}$, for a single cell (absorber case) with a δ -shaped source, using polynomial orders $P = 1$ through $P = 4$	30

2.11	Numerical inflow values as a function of $\frac{S_1}{S_0}$, for a single cell (absorber case) with a δ -shaped source, using polynomial orders $P = 1$ through $P = 4$	31
2.12	Numerical inflow values as a function of $\frac{S_1}{S_0}$, for a single cell (absorber case) with a δ -shaped source, using polynomial orders $P = 1$ through $P = 4$	31
2.13	Convergence rate of the L_2 norm of the error, E_ψ , as a function of the mesh cell size for a pure absorber ($\sigma_t(x) = 1$ [cm^{-1}] and $x \in [0, 10$ [cm]]).	37
2.14	Convergence rate of the L_2 norm of the error, E_ψ , as a function of the mesh cell size for a pure absorber ($\sigma_t(x) = 1$ [cm^{-1}] and $x \in [0, 10$ [cm]]).	38
2.15	Convergence rate of the L_2 norm of the error, E_ψ , as a function of the mesh cell size for a pure absorber ($\sigma_t(x) = 1$ [cm^{-1}] and $x \in [0, 10$ [cm]]).	39
2.16	Convergence rate of the L_2 norm of the error, E_ψ , as a function of the mesh cell size for a pure absorber ($\sigma_t(x) = 1$ [cm^{-1}] and $x \in [0, 10$ [cm]]).	40
2.17	Convergence rate for $E_{\psi,A}$ as a function of the mesh cell size for a homogeneous pure absorber and linear DFEM.	41
2.18	Convergence rate for $E_{\psi,A}$ as a function of the mesh cell size for a homogeneous pure absorber and quadratic DFEM.	42
2.19	Convergence rate for $E_{\psi,A}$ as a function of the mesh cell size for a homogeneous pure absorber and cubic DFEM.	43
2.20	Convergence rate for $E_{\psi,A}$ as a function of the mesh cell size for a homogeneous pure absorber and quartic DFEM.	44
2.21	Convergence rate of $E_{\psi,out}$ as a function of the mesh cell size for a homogeneous pure absorber for linear DFEM.	45
2.22	Convergence rate of $E_{\psi,out}$ as a function of the mesh cell size for a homogeneous pure absorber for quadratic DFEM.	46
2.23	Convergence rate of $E_{\psi,out}$ as a function of the mesh cell size for a homogeneous pure absorber for cubic DFEM.	47
2.24	Convergence rate of $E_{\psi,out}$ as a function of the mesh cell size for a pure absorber for quartic DFEM.	48
3.1	TAMU figure	51

A.1	TAMU figure	61
B.1	TAMU figure	63

LIST OF TABLES

TABLE		Page
2.1	Nomenclature of numerical schemes (TL=Traditional Lumping; SL=Self-Lumping).	9
2.2	Accuracy of self-Lumping quadratures for trial spaces of different polynomial degree P (each quadrature uses $N_P = P + 1$ points).	17
2.3	Equivalence of traditional lumping and Newton-Cotes approximation of the mass matrix.	19
2.4	Local truncation error analysis in $\tilde{\psi}_{in,d}$ for a single cell problem with constant cross section. Values given as $q(C)$ are to be read as Ch^q with $h = \sigma_t \Delta x / \mu$	32
2.5	Local truncation error analysis in $\tilde{\psi}_{A,d}$ for a single cell problem with constant cross section. Values given as $q(C)$ are to be read as Ch^q with $h = \sigma_t \Delta x / \mu$. “Machine Precision” entries are meant to indicate that Taylor series analysis was inconclusive due to all coefficients being within machine precision.	33
2.6	Local truncation error analysis in $\tilde{\psi}_{out,d}$ for a single cell with constant cross section. Values given as $q(C)$ are to be read as Ch^q with $h = \sigma_t \Delta x / \mu$. “Machine Precision” entries are meant to indicate that Taylor series analysis was inconclusive due to all coefficients being within machine precision.	34
3.1	This is a table template	51

1. INTRODUCTION

This dissertation is dedicated to the solution of thermal radiative transfer (TRT) equations. The TRT equations:

$$\frac{1}{c} \frac{dI}{dt} + \vec{\Omega} \cdot \vec{\nabla} I + \sigma_t I = \int_0^\infty \int_{4\pi} \sigma_s(\vec{\Omega}' \rightarrow \vec{\Omega}, E' \rightarrow E) I, d\vec{\Omega}' dE' + \sigma_a B \quad (1.1a)$$

$$C_v \frac{dT}{dt} = \int_0^\infty \sigma_a (\phi - 4\pi B) dE, \quad (1.1b)$$

are a nonlinear system of equations that describe the exchange of energy between a photon radiation field and a non-moving material. The radiation intensity, I , is a seven dimensional field dependent upon spatial location, \vec{x} ; photon energy, E ; photon direction of travel, $\vec{\Omega}$; and time t . c is the speed of light. Material opacities for all interactions, σ_t ; absorption, σ_a ; and scattering, σ_s are functions of photon energy and material temperature, T . Material heat capacity, C_v , is also a function of material temperature. The angle integrated radiation intensity is an integral over all photon directions of the the photon intensity and is a function of space and photon energy. Finally, the Planck function, B , is a function of photon energy and material temperature. While materials at all temperatures emit photon radiation, the radiation emission is proportional to T^4 . Thus, solution of the radiative transfer equations is most important in situations where materials are very hot. Solving the thermal radiative transfer equations is an important component of the simulation of different scientific and engineering problems including astrophysics supernova explosions and high energy density laboratory physics experiments like those conducted at the National Ignition Facility.

1.1 Simplifications of the Thermal Radiative Transfer Equations

In this dissertation, we make a number of simplifying assumptions to make solution of Eqs. (1.1) more tractable. First, we limit our focus to 1-D Cartesian (slab) geometry. The assumption of slab geometry is not required, but slab geometry radiation transport simulations require significantly less computational time. Further, any methods that have a possibility of being viable for radiation transport in multiple spatial dimensions must also work well in slab geometry.

Second, we approximate the continuous angle dependence of the intensity using the discrete ordinates (S_N) method. The S_N method approximates the true definition of the angle integrated intensity,

$$\phi(\vec{x}, E, t) = \int_{4\pi} I(\vec{x}, \vec{\Omega}, E, t) d\vec{\Omega},$$

using quadrature integration,

$$\phi(\vec{x}, E, t) \approx \sum_{d=1}^{N_{dir}} w_d I(\vec{x}, \vec{\Omega}_d, E, t). \quad (1.2)$$

In Eq. (1.2), $\{w_d, \vec{\Omega}_d\}_{d=1, \dots, N_{dir}}$ is the set of N_{dir} quadrature weights w_d and discrete directions, $\vec{\Omega}_d$ and corresponding intensities I_d .

Finally, we treat the photon energy dependence using the multi-frequency method. The multi-frequency method approximates photon energy dependence by discretizing the continuous photon energy dependence with G discrete groups such that:

$$\int_0^\infty I(\vec{x}, \vec{\Omega}, t, E) dE = \sum_{g=1}^G I_g, \quad (1.3)$$

where

$$I(\vec{x}, \vec{\Omega}, t)_g = \int_{E_{g+1/2}}^{E_{g-1/2}} I(\vec{x}, \vec{\Omega}, t, E) dE, \quad (1.4)$$

$E_{g+1/2}$ is the lower photon energy bound of group g , $E_{g-1/2}$ is the upper photon energy bound of group g , and we have maintained the traditional neutron transport number of higher energy particles belonging to lower number energy groups.

1.2 Spatial and Temporal Discretization

To complete a description of the approach we will take to solve Eqs. (1.1), we now describe how we will discretize the spatial and temporal variables.

1.2.1 Time Integration

The appearance of the speed of light in Eq. (1.1) results in the TRT equations being very stiff. To solve the such a stiff system of equations would require either an impractically small time step, or the use of implicit methods. We elect to use Diagonally Implicit Runge-Kutta (DIRK) methods to advance our TRT solution in time. The simplest of DIRK scheme is the first order implicit Euler scheme, but more advanced DIRK higher order methods in time [5].

1.2.2 Spatial Discretization with Discontinuous Finite Elements

The linear discontinuous finite element method (LDFEM) has long been used to solve the discrete ordinates neutron transport equation [21]. Through manipulation, the thermal radiative transfer equations can be transformed into a form that is equivalent to the neutron transport equation with pseudo- scattering, fission, and fixed sources. This makes it possible to use the same methods and techniques developed for neutron transport to assist in solving the thermal radiative transfer equations. LDFEM has achieved wide spread acceptance in the neutron transport community because it is accurate [12] and highly damped. Because it possesses the thick diffusion

limit [11], LDFEM has also been applied to the S_N TRT equations. Morel, Wareing, and Smith first considered the application of LDFEM to the S_N TRT equations in [17]. Mass matrix lumped LDFEM was shown to preserve the thick equilibrium diffusion limit [17]. This suggests that discontinuous finite element (DFEM) schemes can be used to accurately solve the TRT equations in both diffusive and transport effects dominated regions.

1.3 Progression Towards Higher Order DFEM Thermal Radiative Transfer

For higher order (quadratic and higher polynomial degree trial spaces) DFEM to be accurate and practical for solving Eqs. (1.1) we must demonstrate that higher order DFEM:

1. are “robust”,
2. account for within cell spatial variation of opacity accurately, and
3. can be accelerated using appropriate iterative acceleration techniques.

By “robust”, we mean that that calculated radiation outflow from a spatial cell is strictly positive for all cell widths and optical thicknesses.

In Section 2 we use a steady-state, mono-energetic, source-free pure absorber neutron transport problem with a cross section that is constant in space to examine the robustness of different radiation transport DFEM matrix lumping techniques. Next, we extend the techniques developed by Adams [2, 4], for a spatial discretization scheme related to LDFEM to address the within cell spatial variation of opacity, for higher order DFEM in Section 3. Then, we examine iterative acceleration techniques compatible with higher order DFEM spatial discretizations that account for the spatial variation of interaction cross (in neutron transport problems) or opacity (TRT simulations) in Section 4.

In preparation for solving the coupled, non-linear TRT equations, in Section 5 we combine all of the strategies we have developed in Sections 2-4 and apply them to a coupled system of linear equations. Section 5, is devoted to the development and solution of a two-group fuel depletion problem that uses explicit Euler time differencing. Finally, in Section 6 we solve the energy integrated, or grey, thermal radiative transfer equations using higher order DFEM. We then provides solutions to analytic benchmarks to verify our methods [23], and use the method of manufactured solutions [22] to demonstrate the increased accuracy of applying higher order DFEM and DIRK time integration techniques to the grey TRT equations.

2. DISCONTINUOUS FINITE ELEMENTS FOR RADIATION TRANSPORT

In Section 1, we briefly mentioned that through manipulation, the thermal radiative transfer equations can be put into a form equivalent to the neutron transport equations with pseudo-scattering, fission, and fixed sources. We will (repeatedly) go through this process in Section 6, but for now we take for granted that solving for the neutron transport equation's angular flux, ψ , is related to solving Eq. (1.1) for I . Additionally, we will assume that a steady-state neutron transport source-free pure absorber problem taxes DFEM schemes in a manner similar to the way DFEM schemes are tested in time-dependent thermal radiative transfer simulations, in particular Marshak wave type problems [19]

2.1 History of DFEM for Neutron Transport

The linear discontinuous finite element method (LDFEM) for discrete ordinates neutron transport is widely used and has been extensively studied [10, 6, 15, 3]. However, the DFEM technique is not limited to linear trial spaces. Reed et. al [21] used arbitrary order DFEM S_N transport in TRIPLET but, due to data storage limitations at the time, only LDFEM was computationally practical. Possibly as a result of these historical computing limitations, the majority of reported DFEM radiation transport literature has focused on the LDFEM approximation. Higher order DFEM methods have received periodic attention; some older examples include the work of Walters [25] and Hennart and del Valle [8, 9]. More recent investigations of higher order DFEM trial spaces include those of Warsa and Prinja [28] and Wang and Ragusa [27, 26]. The primary focus of the work in [8, 9, 28, 27, 26] was the convergence rate of arbitrary order DFEM schemes.

Negative angular flux solutions of the neutron transport equation obtained with

LDFEM have been well documented in [6, 15, 3]. While these negativities do not affect the order of convergence and can be tolerated for certain applications [13], some nonlinear problems, particularly radiative transfer calculations, can diverge if the angular intensities are negative. As a result, several methods to eliminate or inhibit negative solutions have been developed and can be categorized into one of three categories: ad-hoc fix-ups [6], strictly non-negative solution representations [15], and matrix lumping [3]. The first two methods result in nonlinear systems of equations, while matrix lumping yields linear systems of equations. By definition, ad-hoc fix-ups and strictly non-negative solution representations yield non-negative outflows in 1-D, 2-D, and 3-D geometries, regardless of material properties. Mass matrix lumping (applied to LDFEM) yields strictly positive outflows only in 1-D geometries, though it does otherwise inhibit negativities [3]. Although not related to DFEM discretizations, we note that other approaches have been investigated to mitigate negativities; see, for instance, [7].

Solution positivity of even degree unlumped DFEM methods for 1-D problems has been noted previously [25, 8, 9]. In comparing DFEM methods to nodal transport methods, Walters derived the quadratic DFEM scheme from the nodal transport equations using the Padé(2,3) approximation to the exponential term and noted that this approximation would result in a strictly positive outflow, regardless of cell optical thickness [25]. Hennart and del Valle then showed for slab geometry that all even P degree polynomial DFEM schemes approximate the cell outflow angular flux as a Padé($P, P + 1$) function, which is a strictly positive approximation of the exponential [8, 9]. The positivity of even degree unlumped DFEM for 1-D problems was also shown in [28].

2.2 Matrix Lumping Techniques to Study

In this Section, we examine the idea of mass matrix lumping and its ability to ensure positive angular flux solutions of the neutron transport equation for arbitrary degree DFEM trial spaces in non-scattering 1-D slab geometries. We consider traditional lumping (TL), that constructs a diagonal mass matrix by collapsing all off-diagonal entries onto the main diagonal [3], and quadrature-based self-lumping (SL) methods [20], that yield a diagonal mass matrix by numerically integrating the DFEM equations using the DFEM interpolatory points as quadrature points. Restricting ourselves to equally-spaced interpolation points, self-lumping numerical integration with the greatest degree of accuracy is achieved through the use of closed Newton-Cotes formulae [1]. However, Newton-Cotes formulas with a large number of integration points are known to be oscillatory and are of relatively low-order accuracy, integrating polynomials at most of degree equal to the number of integration points. By considering solution representations that employ quadrature points as the interpolatory points, for example Gauss-Legendre (hereafter Gauss) or Lobatto-Gauss-Legendre (hereafter Lobatto) quadrature points [1], we wish to find methods that are self-lumping with a significantly higher accuracy. We analyze the combinations of Lagrange interpolatory points and numerical integration strategies given in Table 2.1 for positivity of the angular flux solution, local truncation error order, and spatial convergence order as a function of trial space polynomial degree. We limit the consideration of exact numerical integration schemes to those with equally-spaced interpolatory points, due to the fact that exact integration with any particular set of interpolatory points will always yield the same DFEM solution)

It has long been noted that traditional lumping (TL) with equally-spaced interpolatory points for 1-D LDFEM is equivalent to using the trapezoidal quadrature

Table 2.1: Nomenclature of numerical schemes (TL=Traditional Lumping; SL=Self-Lumping).

Interpolation Point Type	Integration Strategy	Method Short Hand Name
Equally- Spaced	Exact spatial integration, with collapsing of mass matrix entries to the main diagonal	TL
Equally- Spaced	Numerical integration via Newton-Cotes quadrature restricted to interpolation points	SL Newton-Cotes
Gauss Quadrature	Numerical integration via Gauss quadrature restricted to interpolation points	SL Gauss
Lobatto Quadrature	Numerical integration via Lobatto quadrature restricted to interpolation points	SL Lobatto
Equally- Spaced	Exact spatial integration	Exact DFEM

rule to approximately integrate the mass matrix [24] while exactly integrating the gradient operator. Since the trapezoidal rule is identical to the closed Newton-Cotes formula with two points, we hypothesize that, for finite elements of arbitrary order using equally-spaced interpolatory points, traditional lumping is equivalent to using a closed Newton-Cotes formula to compute the mass matrix while exactly integrating the gradient operator. We demonstrate the equivalence between traditional lumping and closed Newton-Cotes formulae in the computation of the mass matrix.

Self-lumping (SL) based on Newton-Cotes formulae differs from traditional lumping in that SL Newton-Cotes generally does not exactly integrate the gradient operator. Coincidentally, the gradient operator is exactly integrated for linear/quadratic trial spaces using a 2-point/3-point Newton-Cotes formula, respectively. However, for higher degree polynomial trial spaces, the corresponding Newton-Cotes formula does not exactly integrate the gradient operator.

Self-lumping based on either Gauss or Lobatto quadratures exactly integrates the gradient operator in 1-D slab geometry for all degree of polynomial trial spaces; thus, there is no need to distinguish between exact integration and quadrature integration of the gradient operator for the SL Gauss and SL Lobatto schemes.

2.3 Lumping Techniques for the 1-D S_N Neutron Transport Equation with Arbitrary Order DFEM

In Sec. 2.3, we provide the weak form for the 1-D S_N equations discretized with DFEM and define the different mass matrix lumping techniques.

2.3.1 Weak Form Derivation

Consider the 1-D slab geometry S_N neutron transport equation:

$$\mu_d \frac{d\psi_d}{dx} + \sigma_t \psi_d = Q_d, \quad (2.1)$$

where ψ_d is the angular flux [$1/[cm^2 - sec - ster]$] in the μ_d direction, μ_d is the d 'th directional cosine relative to the x -axis, σ_t is the total interaction cross section [cm^{-1}], and Q_d is a total source (fixed+scattering+fission) angular source in the direction of μ_d [$1/[cm^3 - sec - ster]$]. In all that follows, we consider only non-scattering, non-fissioning media (pure absorbers), thus Q_d will only be non-trivial if a fixed source is present in the problem. The scalar flux ϕ [$n/cm^2 - sec$] is defined as

$$\phi(x) = 2\pi \int_{-1}^1 \psi(x, \mu_d) d\mu_d. \quad (2.2)$$

For simplicity, we derive the DFEM equations for a single-cell domain, with $x \in [x_L, x_R]$. A known angular flux, $\psi_{in,d}$, is defined on the incoming face of the domain for all μ_d . For $\mu_d > 0$, $\psi_{in,d}$ is defined only at x_L and for $\mu_d < 0$, $\psi_{in,d}$ is defined

at x_R . We begin our derivation by first transforming the physical geometry to a reference element, $s \in [-1, 1]$. This affine transformation is such that:

$$x = \bar{x} + \frac{\Delta x}{2}s \quad (2.3a)$$

$$dx = \frac{\Delta x}{2}ds \quad (2.3b)$$

with $\bar{x} = \frac{x_L + x_R}{2}$ and $\Delta x = x_R - x_L$. We seek a numerical approximation to the true angular flux ψ_d using Lagrange polynomials of degree P :

$$\psi_d(s) \approx \tilde{\psi}_d(s) = \sum_{j=1}^{N_P} \psi_{j,d} \mathbf{B}_j(s), \quad (2.4)$$

where the \sim denotes the numerical approximation. The basis functions \mathbf{B}_j are the canonical Lagrange polynomials

$$\mathbf{B}_j(s) = \prod_{\substack{k=1 \\ k \neq j}}^{N_P} \frac{s - s_k}{s_j - s_k}, \quad (2.5)$$

and $N_P = P + 1$. To determine the N_P unknown coefficients of Eq. (2.4), we follow a standard discontinuous Galerkin procedure, successively multiplying Eq. (2.1) by weight function \mathbf{B}_i and integrating by parts, hence generating N_P moment equations ($1 \leq i \leq N_P$). We assume that the cross sections are constant per cell. Inserting our solution representation $\tilde{\psi}_d$, the i -th moment equation is given by:

$$\begin{aligned} \mu_d \left[\mathbf{B}_i(1)\tilde{\psi}_d(1) - \mathbf{B}_i(-1)\tilde{\psi}_d(-1) - \int_{-1}^1 \tilde{\psi}_d(s) \frac{d\mathbf{B}_i}{ds} ds \right] + \frac{\Delta x \sigma_t}{2} \int_{-1}^1 \mathbf{B}_i(s) \tilde{\psi}_d(s) ds \\ = \frac{\Delta x}{2} \int_{-1}^1 \mathbf{B}_i(s) Q_d(s) ds. \end{aligned} \quad (2.6)$$

We now introduce the upwind approximation to define the angular flux at the cell edges. For $\mu_d > 0$ the angular flux at the cell interfaces is

$$\tilde{\psi}_d(-1) = \psi_{in,d} \quad (2.7a)$$

$$\tilde{\psi}_d(1) = \sum_{j=1}^{N_P} \psi_{j,d} \mathbf{B}_j(1). \quad (2.7b)$$

Similarly for $\mu_d < 0$:

$$\tilde{\psi}_d(-1) = \sum_{j=1}^{N_P} \psi_{j,d} \mathbf{B}_j(-1) \quad (2.8a)$$

$$\tilde{\psi}_d(1) = \psi_{in,d}. \quad (2.8b)$$

In Eq. (2.7a) and Eq. (2.8b), $\psi_{in,d}$ is either the known angular flux outflow from the upwind cell or a boundary condition. Inserting the definition of $\tilde{\psi}_d(s)$, Eq. (2.6) becomes, for $\mu_d > 0$,

$$\begin{aligned} \mu_d \left[\mathbf{B}_i(1) \left(\sum_{j=1}^{N_P} \psi_{j,d} \mathbf{B}_j(1) \right) - \mathbf{B}_i(-1) \psi_{in,d} - \int_{-1}^1 \left(\sum_{j=1}^{N_P} \psi_{j,d} \mathbf{B}_j(s) \right) \frac{d\mathbf{B}_i}{ds} ds \right] + \\ \frac{\Delta x \sigma_t}{2} \int_{-1}^1 \mathbf{B}_i(s) \left(\sum_{j=1}^{N_P} \psi_{j,d} \mathbf{B}_j(s) \right) ds = \frac{\Delta x}{2} \int_{-1}^1 \mathbf{B}_i(s) Q_d(s) ds, \quad (2.9) \end{aligned}$$

and, for $\mu_d < 0$,

$$\begin{aligned} \mu_d \left[\mathbf{B}_i(1) \psi_{in,d} - \mathbf{B}_i(-1) \left(\sum_{j=1}^{N_P} \psi_{j,d} \mathbf{B}_j(-1) \right) - \int_{-1}^1 \left(\sum_{j=1}^{N_P} \psi_{j,d} \mathbf{B}_j(s) \right) \frac{d\mathbf{B}_i}{ds} ds \right] \\ + \frac{\Delta x \sigma_t}{2} \int_{-1}^1 \mathbf{B}_i(s) \left(\sum_{j=1}^{N_P} \psi_{j,d} \mathbf{B}_j(s) \right) ds = \frac{\Delta x}{2} \int_{-1}^1 \mathbf{B}_i(s) Q_d(s) ds. \quad (2.10) \end{aligned}$$

Considering all of the N_P moment equations at once we can write both Eq. (2.9) and Eq. (2.10) in a single matrix form:

$$\left(\mu_d \mathbf{G} + \frac{\sigma_t \Delta x}{2} \mathbf{M} \right) \vec{\psi}_d = \frac{\Delta x}{2} \vec{Q}_d + \mu_d \psi_{in,d} \vec{f}. \quad (2.11)$$

In Eq. (2.11) we have made use of the following definitions: the vector of unknowns is given by

$$\vec{\psi}_d = [\psi_{1,d} \ \dots \ \psi_{N_P,d}]^T, \quad (2.12)$$

the mass matrix \mathbf{M} is:

$$\mathbf{M}_{ij} = \int_{-1}^1 \mathbf{B}_i(s) \mathbf{B}_j(s) ds, \quad (2.13)$$

the fixed source moment vector, \vec{Q}_d , is a column vector of length N_P :

$$\vec{Q}_{d,i} = \int_{-1}^1 \mathbf{B}_i(s) Q_d(s) ds, \quad (2.14)$$

and \vec{f} is a column vector of length N_P :

$$\vec{f}_i = \begin{cases} \mathbf{B}_i(-1) & \text{for } \mu_d > 0 \\ -\mathbf{B}_i(1) & \text{for } \mu_d < 0 \end{cases}. \quad (2.15)$$

\mathbf{G} is a $N_P \times N_P$ matrix which we refer to as the gradient operator. When $\mu_d > 0$, \mathbf{G} is given by:

$$\mathbf{G}_{ij} = \mathbf{B}_i(1) \mathbf{B}_j(1) - \int_{-1}^1 \frac{d\mathbf{B}_i}{ds} \mathbf{B}_j(s) ds. \quad (2.16a)$$

For $\mu_d < 0$, \mathbf{G} is:

$$\mathbf{G}_{ij} = -\mathbf{B}_i(-1) \mathbf{B}_j(-1) - \int_{-1}^1 \frac{d\mathbf{B}_i}{ds} \mathbf{B}_j(s) ds. \quad (2.16b)$$

When interpolatory points are not located at the cell interfaces (i.e., at $s = \pm 1$), it can be noted that

1. \vec{f} has N_P non-zero entries, and
2. $\mathbf{B}_i(\pm 1)\mathbf{B}_j(\pm 1) \neq 0$ for all $i, j = 1, \dots, N_P$.

When a Lagrange interpolatory point exists on the cell edges, then \vec{f} has only one non-zero entry and the product $\mathbf{B}_i(\pm 1)\mathbf{B}_j(\pm 1) \neq 0$ only when $i = j = N_P$ for $\mu_d > 0$ or when $i = j = 1$ for $\mu_d < 0$, as is the case when equally-spaced points or a Lobatto quadrature are used as interpolation points.

We evaluate the integrals of Eq. (2.13) and Eq. (2.16) using a numerical quadrature. A method exactly integrates a quantity when the quadrature rule used to evaluate the integral is accurate for polynomials of degree equal to or greater than the polynomial degree of the integrand. In general, the matrices are dense and their entries are computed as:

$$\mathbf{M}_{ij} \approx \sum_{q=1}^{N_q} w_q \mathbf{B}_i(s_q) \mathbf{B}_j(s_q) \quad (2.17)$$

$$\mathbf{G}_{ij} \approx sg(\mu_d) \mathbf{B}_i(sg(\mu_d)) \mathbf{B}_j(sg(\mu_d)) - \sum_{q=1}^{N_q} w_q \left. \frac{d\mathbf{B}_i}{ds} \right|_{s=s_q} \mathbf{B}_j(s_q), \quad (2.18)$$

where N_q is the number of quadrature points to be used, w_q are the weights associated with quadrature points s_q , and $sg(a)$ is the sign function defined as

$$sg(a) = \begin{cases} +1 & \text{if } a > 0 \\ -1 & \text{if } a < 0 \end{cases}. \quad (2.19)$$

2.3.2 Traditional Lumping

The traditional lumping (TL) scheme replaces \mathbf{M} with $\widehat{\mathbf{M}}$, the latter being formed by collapsing row entries onto the main diagonal via the following formula [3]:

$$\widehat{\mathbf{M}}_{ij} = \begin{cases} \sum_{j=1}^{N_P} \mathbf{M}_{ij} & \text{for } i = j \\ 0 & \text{otherwise} \end{cases}. \quad (2.20)$$

2.3.3 Quadrature-Based Lumping

An alternative method of mass matrix lumping restricts the quadrature points to the interpolatory points where:

$$\mathbf{B}_i(s_j) = \begin{cases} 1 & \text{if } s_i = s_j \\ 0 & \text{otherwise} \end{cases}, \quad i = 1, \dots, N_P, \quad (2.21)$$

and the quadrature integration of Eq. (2.17) reduces to:

$$\mathbf{M}_{ij} = \begin{cases} w_i & i = j \\ 0 & \text{otherwise} \end{cases}. \quad (2.22)$$

As mentioned previously, we refer to the implicit lumping of Eq. (2.22) as self-lumping (SL). Self-lumping is a method to automatically generate a diagonal mass matrix. We note that self-lumping does not imply that the quadrature formula inexactly integrates the mass matrix.

2.3.4 Source Moment Evaluation

Historically, when discussing lumping techniques, the focus has been on matrix lumping [3] and little attention was paid to lumping source terms. For instance,

we consider δ -shaped volumetric sources (i.e., equal to 0 everywhere except at one given point) as an example of a highly skewed volumetric source. In such a case, the evaluation of \vec{Q}_d using quadrature-based self-lumping schemes is an open question. Obviously, quadrature-based schemes cannot evaluate Eq. (2.14) for δ -sources. To address this, we expand the source on a Legendre polynomial basis:

$$\hat{S}_d(s) = \sum_{n=0}^P S_n P_n(s) \quad (2.23a)$$

$$\text{with } S_n = \frac{2n+1}{2} \int_{-1}^1 Q_d(s) P_n(s) ds, \quad (2.23b)$$

and evaluate \vec{Q}_d as follows

$$\vec{Q}_{d,i} = \int_{-1}^1 \mathbf{B}_i(s) \hat{S}_d(s) ds. \quad (2.24)$$

Note that if the right-hand-side of Eq. (2.24) is exactly integrated, this is equivalent to exactly integrating Eq. (2.14).

2.4 Quadrature Point Selection

In Sec. 2.4, we discuss the properties of different numerical quadratures as applied to the 1-D DFEM S_N equations.

We consider three different types of interpolatory points: equally-spaced, Gauss quadrature, and Lobatto quadrature. On the $[-1, 1]$ interval, the $N_P = P+1$ equally spaced interpolation points for a degree P polynomial trial space are:

$$s_j = -1 + (j-1) \frac{2}{P}, \quad j = 1, \dots, N_P. \quad (2.25)$$

Self-lumping using equally-spaced interpolation points requires numerical integration with closed Newton-Cotes quadrature formulae. The N_P weights, w_j , used for

Newton-Cotes numerical integration at the interpolation points do not follow a concise pattern, so we refer the reader to [1]. The Gauss quadrature points are the N_P roots of the Legendre polynomial, $P_{N_P}(s)$ [1]. The corresponding weights are:

$$w_j = \frac{2}{(1 - s_j^2)} [P'_{N_P}(s_j)]^2 . \quad (2.26)$$

Lobatto quadrature points have fixed endpoints, $s_1 = -1$, $s_{N_P} = 1$. The remaining $N_P - 2$ points are the roots of $P'_{N_P-1}(s)$ [1], with corresponding weights:

$$w_j = \begin{cases} \frac{2}{N_P(N_P-1)} & j = 1, j = N_P \\ \frac{2}{N_P(N_P-1)[P'_{N_P-1}(s_j)]^2} & \text{otherwise} \end{cases} . \quad (2.27)$$

The highest polynomial degree a particular self-lumping quadrature formula exactly integrates is given in Table 2.2 for Newton-Cotes, Gauss, and Lobatto quadratures. Also listed in Table 2.2 is the maximum polynomial degree of the integrands present in the gradient and mass matrices.

Table 2.2: Accuracy of self-Lumping quadratures for trial spaces of different polynomial degree P (each quadrature uses $N_P = P + 1$ points).

Polynomial Degree of $\tilde{\psi}$	$N_P =$ $P + 1$	Degree of M integrand	Degree of G integrand	Accuracy of Newton-Cotes	Accuracy of Gauss	Accuracy of Lobatto
1	2	2	1	1	3	1
2	3	4	3	3	5	3
3	4	6	5	3	7	5
4	5	8	7	5	9	7
5	6	10	9	5	11	9
P	$P + 1$	$2P$	$2P - 1$	Odd $\tilde{\psi}$: P Even $\tilde{\psi}$: $P + 1$	$2P + 1$	$2P - 1$

Since the accuracy of an $N_P = P + 1$ point Gauss quadrature integration exceeds the polynomial degree of the \mathbf{M} and \mathbf{G} integrands for a trial space of degree P , using the SL Gauss scheme will strictly yield the same numerical solution as any DFEM scheme that exactly integrates \mathbf{M} and \mathbf{G} . Thus, the SL Gauss scheme yields the same numerical solution as the Exact DFEM scheme.

For linear and quadratic trial spaces, self-lumping methods using either Lobatto or equally-spaced interpolation points will yield identical solutions. This is a direct result of the two- and three-point Lobatto quadrature formulae being identical to the two- and three-point closed Newton-Cotes quadratures. This equivalence does not hold for higher degree polynomial trial spaces because the Lobatto quadrature points will no longer correspond to the equally-spaced quadrature points.

By definition, TL uses equally-spaced interpolation points and exactly integrates the gradient operator. For cell-wise constant cross sections, TL is equivalent to a numerical integration scheme that:

1. uses equally-spaced interpolation points,
2. integrates the gradient operator exactly, and
3. uses a Newton-Cotes quadrature restricted to the DFEM interpolation points to compute the mass matrix.

The third point can easily be demonstrated. Indeed, with traditional lumping, \mathbf{M}_{ij} is exactly computed and then a row-sum operation is performed on the rows of \mathbf{M} ; thus the entries of the diagonal mass matrix computed for TL are

$$\begin{aligned} \widehat{\mathbf{M}}_{ii} &= \sum_{j=1}^{N_P} \int_{-1}^1 \mathbf{B}_i(s) \mathbf{B}_j(s) \, ds = \int_{-1}^1 \mathbf{B}_i(s) \left[\sum_{j=1}^{N_P} \mathbf{B}_j(s) \right] \, ds \\ &= \int_{-1}^1 ds \, \mathbf{B}_i(s) \quad \forall i = 1, \dots, N_P, \end{aligned} \quad (2.28)$$

because $\sum_j^{N_P} \mathbf{B}_j(s) = 1 \ \forall s \in [-1, +1]$ by definition. The integral $\int_{-1}^1 ds \mathbf{B}_i(s)$ is exactly integrated using a closed Newton-Cotes formula with $N_P = P + 1$ points since $\mathbf{B}_i(s)$ is a polynomial of degree P . Finally, when the \mathbf{B}_i functions are defined using equally-spaced points, the use of a closed Newton-Cotes formula with N_P points yields

$$\widehat{\mathbf{M}}_{ii} = \int_{-1}^1 ds \mathbf{B}_i(s) = \sum_{q=1}^{N_P} w_q \mathbf{B}_i(s_q) = w_i, \quad (2.29)$$

because $\mathbf{B}_i(s_q) = \delta_{iq}$. Thus, the diagonal mass matrix computed using TL contains the closed Newton-Cotes weights as diagonal entries and is equivalent to approximating \mathbf{M} using closed Newton-Cotes quadrature in Eq. (2.22). We also numerically verify this in Table 2.3 for polynomial degrees up to 4.

Table 2.3: Equivalence of traditional lumping and Newton-Cotes approximation of the mass matrix.

P	Exact Integration of \mathbf{M}	Row Sum of \mathbf{M}	Newton-Cotes w with $P + 1$ points
1	$\begin{bmatrix} \frac{2}{3} & \frac{1}{3} \\ \frac{1}{3} & \frac{2}{3} \end{bmatrix}$	$\begin{bmatrix} 1 \\ 1 \end{bmatrix}$	$\begin{bmatrix} 1 \\ 1 \end{bmatrix}$
2	$\begin{bmatrix} \frac{4}{15} & \frac{2}{15} & -\frac{1}{15} \\ \frac{2}{15} & \frac{16}{15} & \frac{1}{15} \\ -\frac{1}{15} & \frac{2}{15} & \frac{4}{15} \end{bmatrix}$	$\begin{bmatrix} \frac{1}{3} \\ \frac{4}{3} \\ \frac{1}{3} \end{bmatrix}$	$\begin{bmatrix} \frac{1}{3} \\ \frac{4}{3} \\ \frac{1}{3} \end{bmatrix}$
3	$\begin{bmatrix} \frac{16}{105} & \frac{38}{280} & -\frac{3}{70} & \frac{19}{840} \\ \frac{33}{280} & \frac{27}{35} & -\frac{27}{280} & -\frac{3}{70} \\ -\frac{3}{70} & -\frac{27}{280} & \frac{27}{35} & \frac{33}{280} \\ \frac{19}{840} & -\frac{3}{70} & \frac{38}{280} & \frac{16}{105} \end{bmatrix}$	$\begin{bmatrix} \frac{1}{4} \\ \frac{3}{4} \\ \frac{3}{4} \\ \frac{1}{4} \end{bmatrix}$	$\begin{bmatrix} \frac{1}{4} \\ \frac{3}{4} \\ \frac{3}{4} \\ \frac{1}{4} \end{bmatrix}$
4	$\begin{bmatrix} \frac{292}{2835} & \frac{296}{2835} & -\frac{58}{945} & \frac{8}{405} & -\frac{29}{2835} \\ \frac{296}{2835} & \frac{256}{405} & -\frac{128}{945} & \frac{256}{2835} & \frac{8}{405} \\ -\frac{58}{945} & -\frac{128}{945} & \frac{208}{315} & -\frac{128}{945} & -\frac{58}{945} \\ \frac{8}{405} & \frac{256}{2835} & -\frac{128}{945} & \frac{256}{405} & \frac{296}{2835} \\ -\frac{29}{2835} & \frac{8}{405} & -\frac{58}{945} & \frac{296}{2835} & \frac{292}{2835} \end{bmatrix}$	$\begin{bmatrix} \frac{7}{45} \\ \frac{32}{45} \\ \frac{4}{15} \\ \frac{32}{45} \\ \frac{7}{45} \end{bmatrix}$	$\begin{bmatrix} \frac{7}{45} \\ \frac{32}{45} \\ \frac{4}{15} \\ \frac{32}{45} \\ \frac{7}{45} \end{bmatrix}$

For linear and quadratic trial spaces, the 2-point and 3-point Newton-Cotes quadrature formulae exactly integrate the gradient operator, as shown in Table 2.2. Thus, for linear and quadratic trial spaces, schemes that use (i) equally-spaced interpolation points and traditional lumping, or (ii) equally-spaced interpolation points and self-lumping numerical integration, or (iii) Lobatto quadrature points as interpolation points and self-lumping numerical integration will yield identical solutions.

2.5 Numerical Results

In this Section, we present numerical results for two 1-D slab problems. For the first problem, we consider a source-free pure absorber with vacuum boundary conditions on the right, a known flux $\psi_{in,d}$ incident on the left face, and a spatially constant total cross section σ_t . The second problem consists of a slab with vacuum boundary conditions on both sides, no scattering, constant σ_t , and a fixed δ -source.

For $\mu_d > 0$, the numerical approximations to the angular flux near the cell inflow and outflow are as follows:

$$\tilde{\psi}_{in,d} = \sum_{j=1}^{N_P} \psi_{j,d} \mathbf{B}_j(-1) \quad (2.30)$$

$$\tilde{\psi}_{out,d} = \sum_{j=1}^{N_P} \psi_{j,d} \mathbf{B}_j(1). \quad (2.31)$$

Regardless of the sign of μ_d , the numerical approximation to the cell average angular flux is defined as:

$$\tilde{\psi}_{A,d} = \frac{1}{2} \sum_{j=1}^{N_P} w_j \psi_{j,d}. \quad (2.32)$$

We used the following quadrature weight normalization: $\sum_{j=1}^{N_P} w_j = 2$. In Eq. (2.30), Eq. (2.31), and Eq. (2.32), $\psi_{j,d}$ are the components of $\vec{\psi}_d$, the numerical solution obtained by solving Eq. (2.11). Hence, the numerical angular flux solution of any

of the previously discussed DFEM schemes can be obtained as a function of h , the number of mean free paths divided by μ_d ,

$$h = \frac{\sigma_t \Delta x}{\mu_d}. \quad (2.33)$$

2.5.1 Incident Flux Single-Cell Outflow Comparison

For the incident-flux problem, the analytical solution of Eq. (2.1) is:

$$\psi(x, \mu_d) = \begin{cases} \psi_{in,d} \exp \left[-\frac{\sigma_t(x-x_L)}{\mu_d} \right] & \text{for } \mu_d > 0 \\ 0 & \text{for } \mu_d < 0 \end{cases}. \quad (2.34)$$

The analytic angular flux outflow, $\psi_{out,d} = \psi(x_R, \mu_d)$, is given by:

$$\psi_{out,d} = \psi_{in,d} \exp[-h]. \quad (2.35)$$

Similarly, the analytic average angular flux within the cell, $\psi_{A,d}$, is:

$$\psi_{A,d} = \frac{1}{\Delta x} \int_{x_L}^{x_R} \psi(x, \mu_d) dx = \frac{\psi_{in,d}}{h} (1 - \exp[-h]). \quad (2.36)$$

The solution components are given by

$$\vec{\psi}_d = \psi_{in,d} \left(\mathbf{G} + \frac{h}{2} \mathbf{M} \right)^{-1} \vec{f}, \quad (2.37)$$

which allows us to compare the various choices of interpolatory points and numerical integration strategies solely as a function of h .

Figures 2.1-2.4 shows the numerically calculated cell outflow, $\tilde{\psi}_{out,d}$, as a function of h for all methods considered. All methods converge to the analytical solution

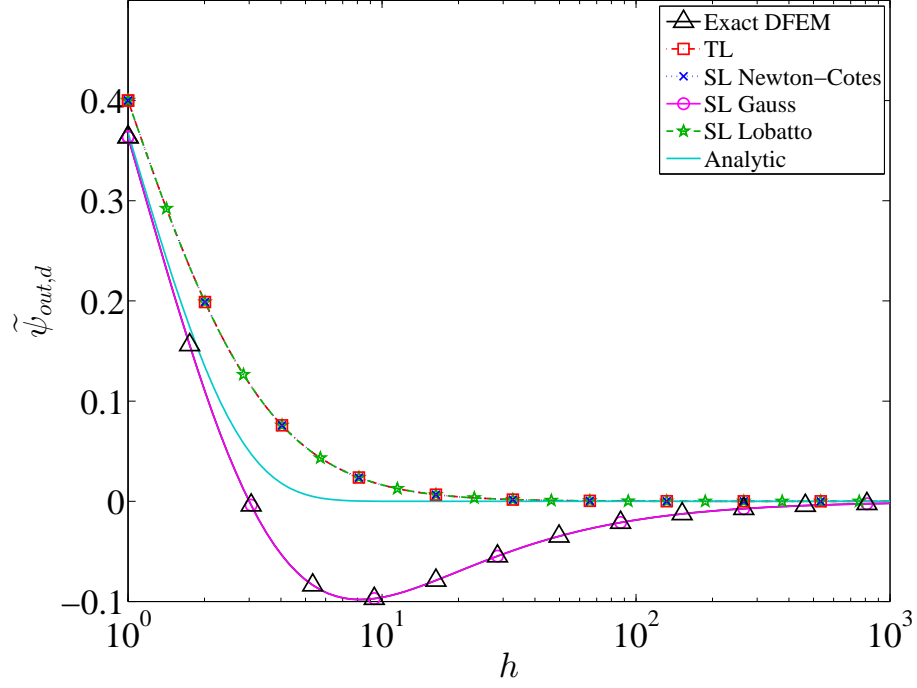


Figure 2.1: Numerical outflow values as a function of h , for a single cell homogeneous absorber problem with a linear DFEM trial space.

as $h \rightarrow 0$, thus we have zoomed in the range where the methods visually differ (i.e., $h \geq 1$). We observe that:

- SL Gauss yields strictly positive outflows for even degree polynomial trial spaces,
- SL Lobatto and SL Newton-Cotes yield strictly positive outflows for odd degree polynomial trial spaces, and
- TL yields strictly positive outflows only for a linear trial space.

We also numerically verify the remarks made in Section 2.4, that is:

- SL Gauss is equivalent to Exact DFEM,

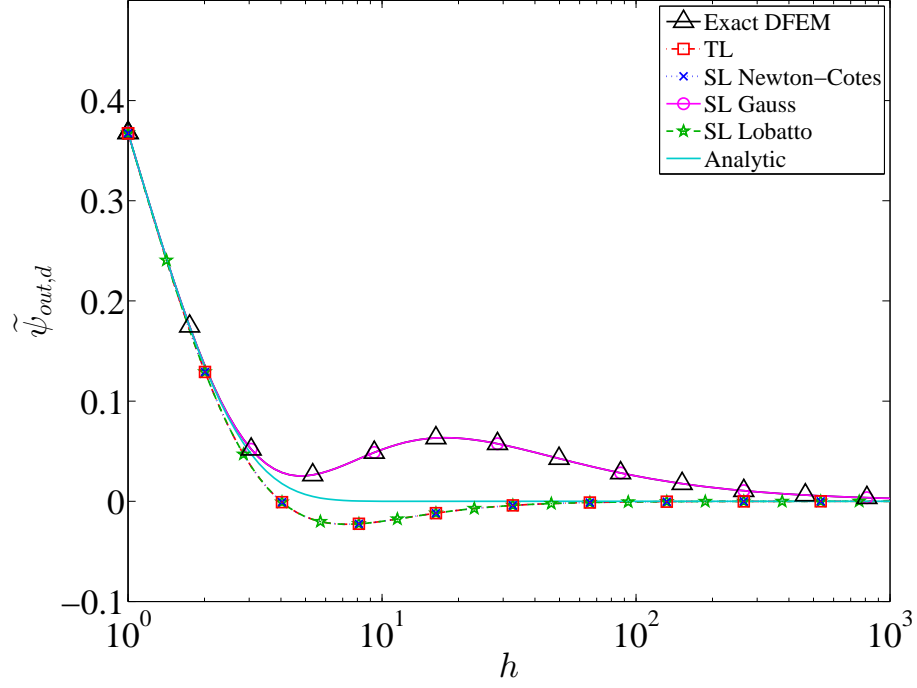


Figure 2.2: Numerical outflow values as a function of h , for a single cell homogeneous absorber problem with a quadratic DFEM trial space.

- SL Lobatto, SL Newton-Cotes, and TL are equivalent for linear and quadratic trial spaces, and
- for even degree trial spaces, the outflow value computed by SL Gauss is not monotonically decreasing as a function of h for cells of intermediate optical thickness (the same was noted in [28] for Exact DFEM).

2.5.2 Fixed Source Single-Cell Inflow Comparison

As noted in [15], it is possible for LDFEM to yield negative solutions near cell inflows for source driven problems. In this second problem, we use a δ -source:

$$Q_d(x) = \begin{cases} \delta(x - x_o) & \text{for } \mu_d > 0 \\ 0 & \text{for } \mu_d < 0 \end{cases}, \quad (2.38)$$

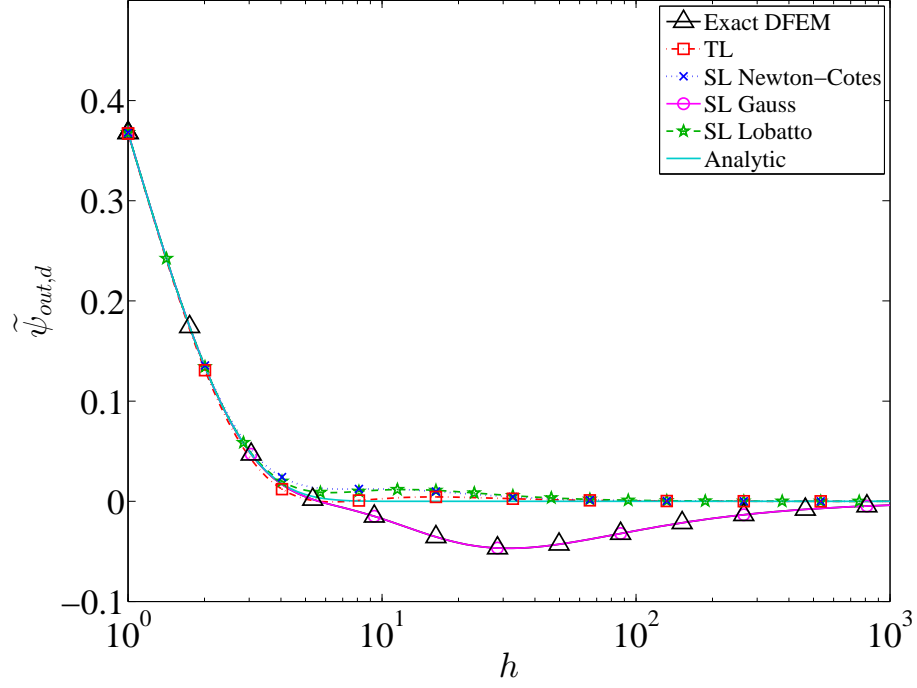


Figure 2.3: Numerical outflow values as a function of h , for a single cell homogeneous absorber problem with a cubic DFEM trial space.

$x \in [-1, 1]$, and $-1 \leq x_o \leq 1$. The analytic solution to this problem for $\mu_d > 0$ is:

$$\psi(x, \mu_d) = \begin{cases} \exp\left[-\frac{\sigma_t(x-x_o)}{\mu_d}\right] & x \geq x_o \\ 0 & x < x_o \end{cases}. \quad (2.39)$$

(For $\mu_d < 0$, $\psi(x, \mu_d) = 0$.) We now examine the numerical approximation to the angular flux near the cell inflow, $\tilde{\psi}_{in,d}$, for various integration schemes, trial space degrees, and as a function of the ratio of the first Legendre moment of the source, S_1 , to the zero-th Legendre moment of the source, S_0 . Note that the physical range of that ratio, $\frac{S_1}{S_0}$, is $[-3, 3]$, corresponding to a δ -source at the left cell edge ($\frac{S_1}{S_0} = -3$) or at the right edge ($\frac{S_1}{S_0} = 3$).

We first consider the case of a vacuum ($\sigma_t = 0$), thus only testing the effect of

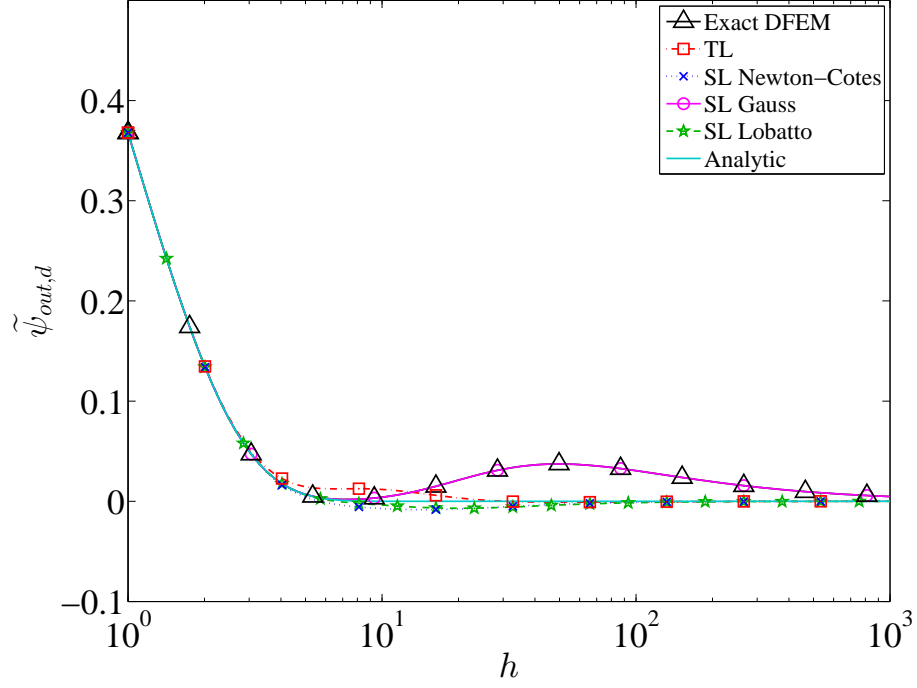


Figure 2.4: Numerical outflow values as a function of h , for a single cell homogeneous absorber problem with a quartic DFEM trial space.

quadrature accuracy in evaluating \vec{Q}_d and \mathbf{G} . In Figs. 2.5-2.8, we plot $\tilde{\psi}_{in,d}$ for three schemes:

1. Lobatto quadrature, which is exact for \mathbf{G} and approximate for the source moments, Eq. (2.24) ,
2. Gauss quadrature: which is exact for both \mathbf{G} and the source moments, and
3. Newton-Cotes quadrature: which is approximate for both \mathbf{G} and the source moments.

The dotted vertical lines in Figs. 2.5-2.8 correspond to the extrema values of $\frac{S_1}{S_0}$ that yield a strictly positive polynomial source representation of degree P (indeed, the degree- P Legendre expansion of the δ -source is not everywhere positive for a

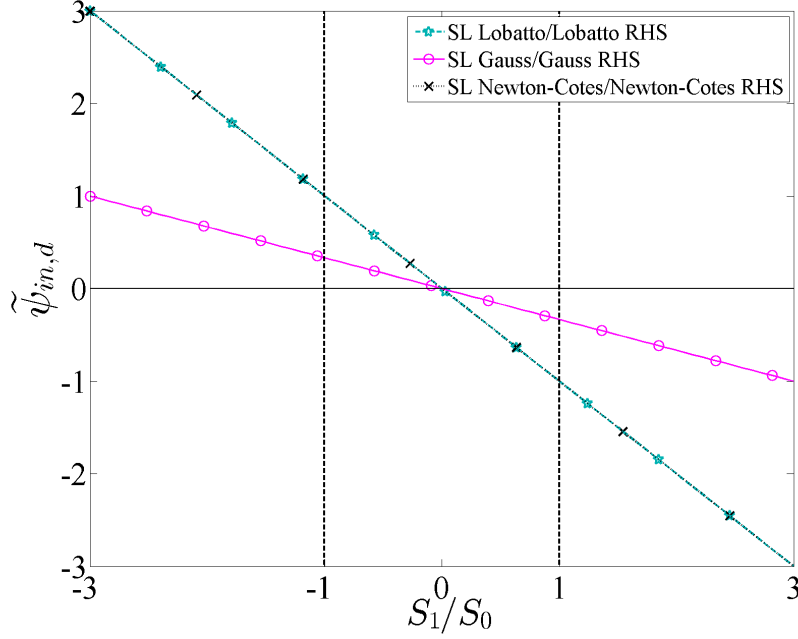


Figure 2.5: Numerical inflow values as a function of $\frac{S_1}{S_0}$ for a single cell (vacuum case) with a δ -shaped source, using polynomial orders $P = 1$ through $P = 4$.

wide range of possible $\frac{S_1}{S_0}$ that are physically realizable). For all trial space degrees, the Gauss scheme exhibits less negativity than either of the other two schemes. The dramatic difference between the Gauss scheme and the Lobatto scheme is solely due to the quadrature formula used to evaluate \vec{Q}_d since both schemes exactly integrate \mathbf{G} . The Newton-Cotes scheme exhibits less severe negativities than the Lobatto scheme but is less robust than the Gauss scheme. Given the results shown in Figs. 2.5-2.8, we conclude that the most robust schemes exactly integrate the source moments, Eq. (2.24).

In Figs. 2.9-2.12, we again examine the positivity of $\tilde{\psi}_{in,d}$, but for a non-vacuum case. The total cell optical thickness was chosen to be 5 mean free paths because this value led to the clearest plots. The relative behaviors observed do not change with cell optical thickness, but using a thicker domain reduces the magnitude for the

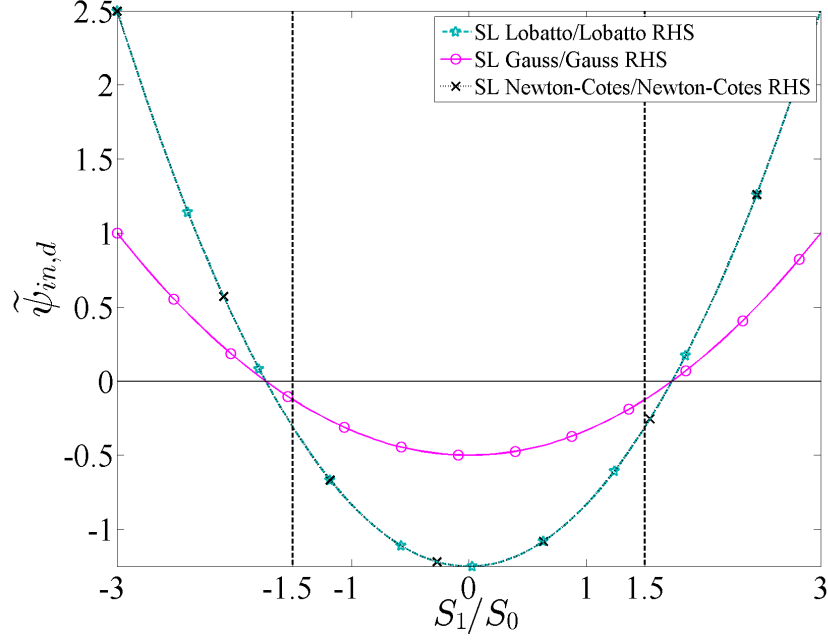


Figure 2.6: Numerical inflow values as a function of $\frac{S_1}{S_0}$ for a single cell (vacuum case) with a δ -shaped source, using polynomial orders $P = 1$ through $P = 4$.

values of $\tilde{\psi}_{in,d}$. All methods in Figs. 2.9-2.12 exactly integrate Eq. (2.24). Regardless of trial space chosen, all schemes exhibit some negativities, but the SL Gauss scheme exhibits the greatest negativities and oscillations. The SL Newton-Cotes scheme presents the least severe negativities.

2.5.3 Single-Cell Taylor Series Analysis

Next, we perform a local truncation error analysis by comparing the Taylor series expansions for the exact and numerical angular fluxes as a function of powers of h for the source-free, incident flux pure absorber problem. Matlab [16] has been employed to perform the symbolic Taylor series expansions about $h = 0$. We denote the Taylor-expanded quantities using the subscript T . The expansions for the analytical inflow,

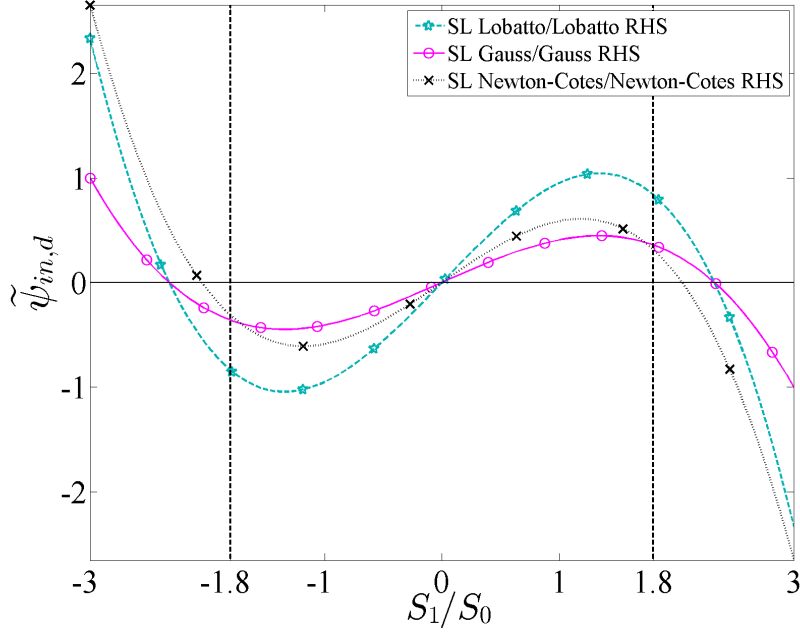


Figure 2.7: Numerical inflow values as a function of $\frac{S_1}{S_0}$ for a single cell (vacuum case) with a δ -shaped source, using polynomial orders $P = 1$ through $P = 4$.

cell average, and outflow are given below:

$$\psi_{in,d,T} = \psi_{in,d} \quad (2.40a)$$

$$\psi_{A,d,T} = \psi_{in,d} \left(1 - \frac{h}{2} + \frac{h^2}{6} - \frac{h^3}{24} + \frac{h^4}{120} - \frac{h^5}{720} \dots \right) \quad (2.40b)$$

$$\psi_{out,d,T} = \psi_{in,d} \left(1 - h + \frac{h^2}{2} - \frac{h^3}{6} + \frac{h^4}{24} - \frac{h^5}{120} \dots \right). \quad (2.40c)$$

The Taylor expansions of the numerical analogues to the quantities in Eqs. (2.40) depend on the trial space polynomial degree, the choice of interpolatory points, and the numerical integration strategy. For brevity, we omit giving these numerical analogues. Table 2.4, Table 2.5, and Table 2.6 give the lowest order h term and the magnitude of its constant (in parenthesis) of the difference between the exact

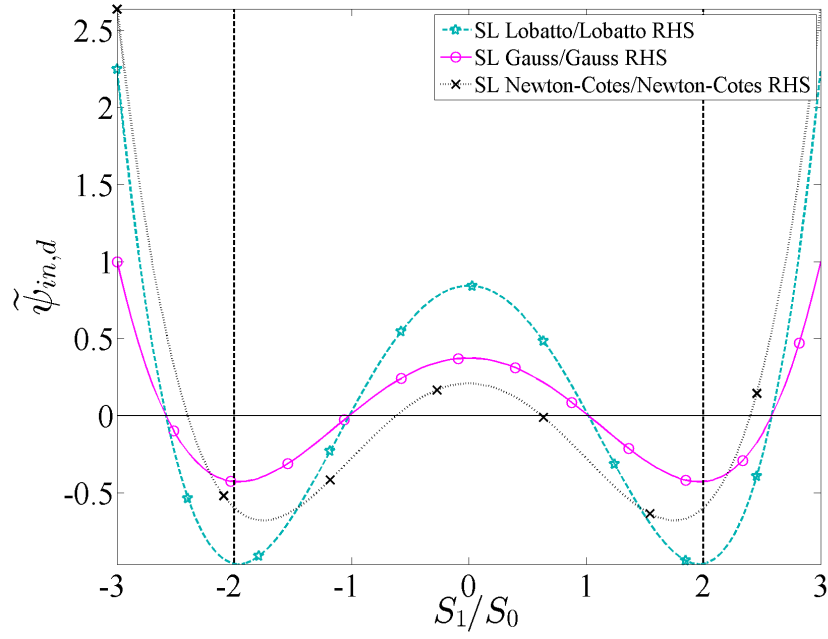


Figure 2.8: Numerical inflow values as a function of $\frac{S_1}{S_0}$ for a single cell (vacuum case) with a δ -shaped source, using polynomial orders $P = 1$ through $P = 4$.

Taylor-expanded quantities and the corresponding Taylor expansions of the numerical approximations to the angular flux near the cell inflow, cell average angular flux, and cell outflow angular flux, respectively.

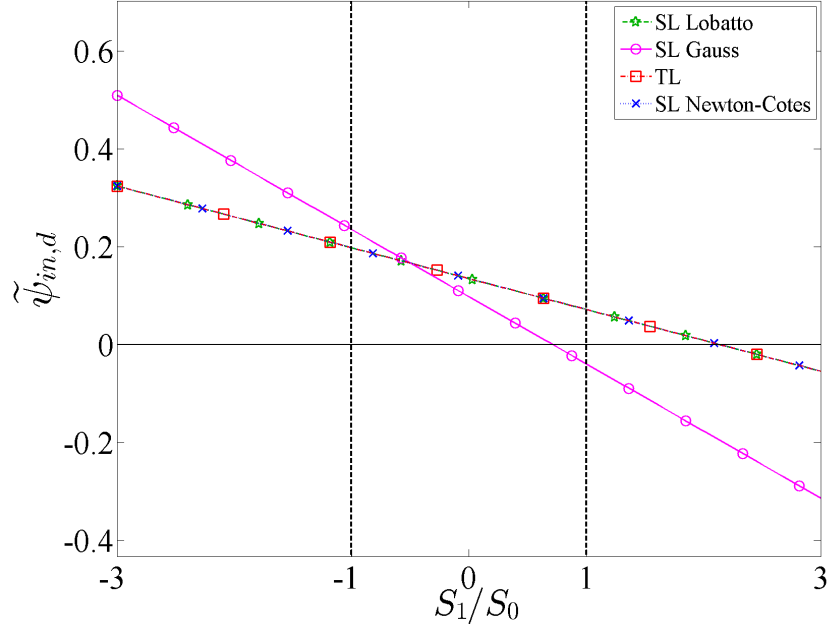


Figure 2.9: Numerical inflow values as a function of $\frac{S_1}{S_0}$, for a single cell (absorber case) with a δ -shaped source, using polynomial orders $P = 1$ through $P = 4$.

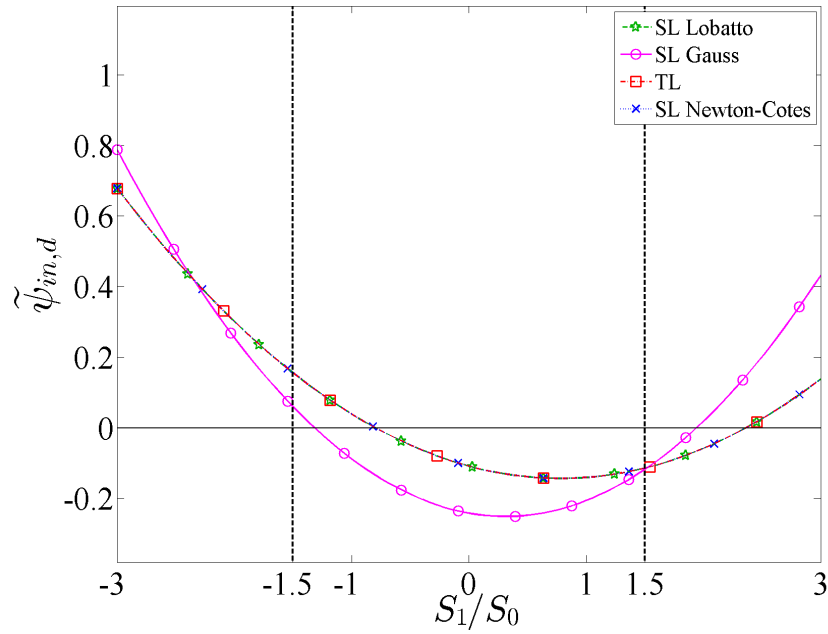


Figure 2.10: Numerical inflow values as a function of $\frac{S_1}{S_0}$, for a single cell (absorber case) with a δ -shaped source, using polynomial orders $P = 1$ through $P = 4$.

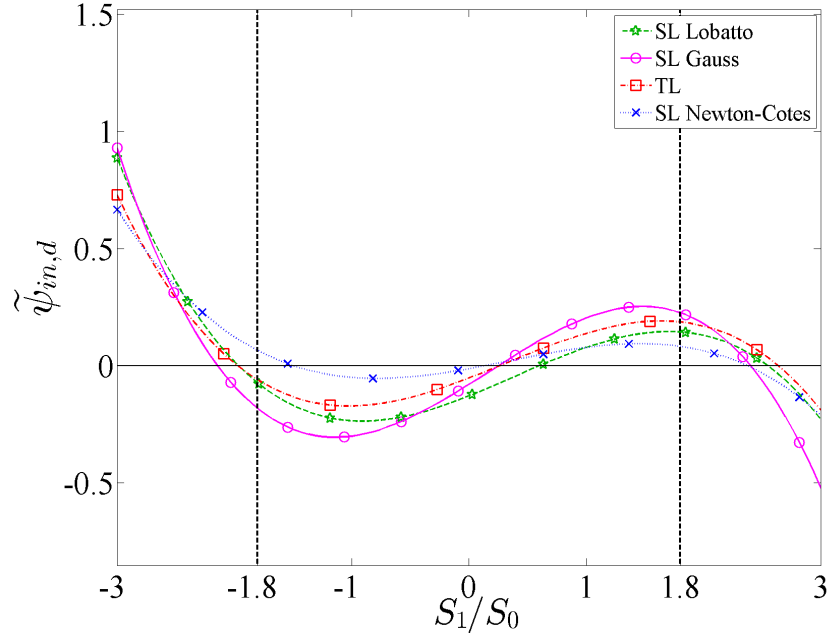


Figure 2.11: Numerical inflow values as a function of $\frac{S_1}{S_0}$, for a single cell (absorber case) with a δ -shaped source, using polynomial orders $P = 1$ through $P = 4$.

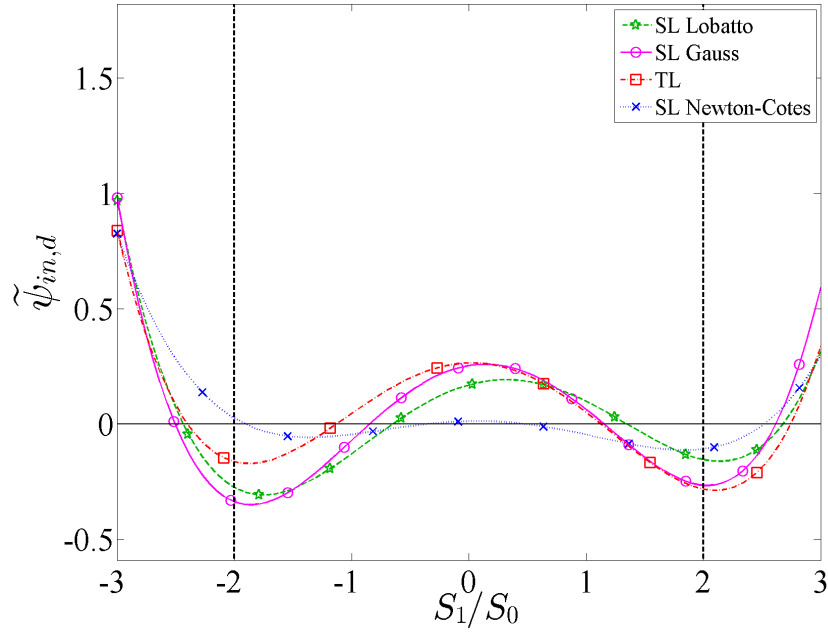


Figure 2.12: Numerical inflow values as a function of $\frac{S_1}{S_0}$, for a single cell (absorber case) with a δ -shaped source, using polynomial orders $P = 1$ through $P = 4$.

Table 2.4: Local truncation error analysis in $\tilde{\psi}_{in,d}$ for a single cell problem with constant cross section. Values given as $q(C)$ are to be read as Ch^q with $h = \sigma_t \Delta x / \mu$.

Polynomial Degree of $\tilde{\psi}$	Exact DFEM	TL	SL Newton-Cotes	SL Gauss	SL Lobatto
1	$2 (2 \times 10^{-1})$	$2 (5 \times 10^{-1})$	$2 (5 \times 10^{-1})$	$2 (2 \times 10^{-1})$	$2 (5 \times 10^{-1})$
2	$3 (2 \times 10^{-2})$	$3 (4 \times 10^{-2})$	$3 (4 \times 10^{-2})$	$3 (2 \times 10^{-2})$	$3 (4 \times 10^{-2})$
3	$4 (1 \times 10^{-3})$	$2 (7 \times 10^{-2})$	$2 (1 \times 10^{-1})$	$4 (1 \times 10^{-3})$	$4 (3 \times 10^{-3})$
4	$5 (7 \times 10^{-5})$	$3 (1 \times 10^{-2})$	$3 (1 \times 10^{-2})$	$5 (7 \times 10^{-5})$	$5 (1 \times 10^{-4})$
5	$6 (3 \times 10^{-6})$	$2 (5 \times 10^{-2})$	$2 (6 \times 10^{-2})$	$6 (3 \times 10^{-6})$	$6 (7 \times 10^{-6})$
6	$7 (1 \times 10^{-7})$	$3 (1 \times 10^{-2})$	$3 (9 \times 10^{-3})$	$7 (1 \times 10^{-7})$	$7 (3 \times 10^{-7})$
7	$8 (4 \times 10^{-9})$	$2 (5 \times 10^{-2})$	$2 (4 \times 10^{-2})$	$8 (4 \times 10^{-9})$	$8 (8 \times 10^{-9})$

Table 2.5: Local truncation error analysis in $\tilde{\psi}_{A,d}$ for a single cell problem with constant cross section. Values given as $q(C)$ are to be read as Ch^q with $h = \sigma_t \Delta x / \mu$. “Machine Precision” entries are meant to indicate that Taylor series analysis was inconclusive due to all coefficients being within machine precision.

Polynomial Degree of $\tilde{\psi}$	Exact DFEM	TL	SL Newton-Cotes	SL Gauss	SL Lobatto
1	$3 (1 \times 10^{-2})$	$2 (2 \times 10^{-1})$	$2 (2 \times 10^{-1})$	$3 (1 \times 10^{-2})$	$2 (2 \times 10^{-1})$
2	$5 (1 \times 10^{-4})$	$4 (2 \times 10^{-3})$	$4 (2 \times 10^{-3})$	$5 (1 \times 10^{-4})$	$4 (2 \times 10^{-3})$
3	$7 (7 \times 10^{-7})$	$3 (3 \times 10^{-3})$	$4 (6 \times 10^{-4})$	$7 (7 \times 10^{-7})$	$6 (1 \times 10^{-5})$
4	$9 (2 \times 10^{-9})$	$5 (8 \times 10^{-5})$	$6 (8 \times 10^{-6})$	$9 (2 \times 10^{-9})$	$8 (5 \times 10^{-8})$
5	$11 (5 \times 10^{-12})$	$3 (1 \times 10^{-3})$	$6 (2 \times 10^{-6})$	$11 (5 \times 10^{-12})$	$10 (1 \times 10^{-10})$
6	$13 (7 \times 10^{-15})$	$5 (7 \times 10^{-5})$	$8 (2 \times 10^{-8})$	$13 (7 \times 10^{-15})$	$12 (2 \times 10^{-13})$
7	Machine Precision	$3 (1 \times 10^{-3})$	$8 (3 \times 10^{-9})$	Machine Precision	Machine Precision

Table 2.6: Local truncation error analysis in $\tilde{\psi}_{out,d}$ for a single cell with constant cross section. Values given as $q(C)$ are to be read as Ch^q with $h = \sigma_t \Delta x / \mu$. “Machine Precision” entries are meant to indicate that Taylor series analysis was inconclusive due to all coefficients being within machine precision.

Polynomial Degree of $\tilde{\psi}$	Exact DFEM	TL	SL Newton-Cotes	SL Gauss	SL Lobatto
1	$4 (1 \times 10^{-2})$	$3 (2 \times 10^{-1})$	$3 (2 \times 10^{-1})$	$4 (1 \times 10^{-2})$	$3 (2 \times 10^{-1})$
2	$6 (1 \times 10^{-4})$	$5 (2 \times 10^{-3})$	$5 (2 \times 10^{-3})$	$6 (1 \times 10^{-4})$	$5 (2 \times 10^{-3})$
3	$8 (7 \times 10^{-7})$	$4 (3 \times 10^{-3})$	$5 (6 \times 10^{-4})$	$8 (7 \times 10^{-7})$	$7 (1 \times 10^{-5})$
4	$10 (2 \times 10^{-9})$	$6 (1 \times 10^{-2})$	$7 (8 \times 10^{-6})$	$10 (2 \times 10^{-9})$	$9 (5 \times 10^{-8})$
5	$12 (5 \times 10^{-12})$	$4 (1 \times 10^{-3})$	$7 (2 \times 10^{-6})$	$12 (5 \times 10^{-12})$	$11 (1 \times 10^{-10})$
6	$14 (7 \times 10^{-15})$	$6 (7 \times 10^{-5})$	$9 (2 \times 10^{-8})$	$14 (7 \times 10^{-15})$	$13 (2 \times 10^{-13})$
7	Machine Precision	$4 (1 \times 10^{-3})$	$9 (3 \times 10^{-9})$	Machine Precision	Machine Precision

This local truncation error analysis illustrates the following.

1. Exact DFEM and SL Gauss, which are equivalent, exactly integrate the mass matrix, and are the most accurate,
2. TL does not guarantee increasing order of accuracy by using higher degree polynomial trial spaces,
3. TL converges at most third or fifth order for $\tilde{\psi}_{A,d}$ and fourth or sixth order for $\tilde{\psi}_{out,d}$ for odd or even polynomial trial spaces, respectively,
4. SL Newton-Cotes increases in accuracy with higher degree polynomial trial spaces, but only for $\tilde{\psi}_{out,d}$ and $\tilde{\psi}_{A,d}$,
5. TL and SL Newton-Cotes are at most second order or third order accurate for $\tilde{\psi}_{in,d}$ for odd or even polynomial trial spaces, respectively,
6. SL Gauss is order $2P+1$ accurate in calculating $\tilde{\psi}_{A,d}$ and order $2P+2$ accurate in calculating $\tilde{\psi}_{out,d}$,
7. SL Lobatto is order $2P$ accurate in calculating $\tilde{\psi}_{A,d}$ and order $2P+1$ in calculating $\tilde{\psi}_{out,d}$,
8. SL Gauss, SL Lobatto, and Exact DFEM are accurate to order $P+1$ in calculating $\tilde{\psi}_{in,d}$, and
9. SL Gauss is more accurate than SL Lobatto (smaller error constant) in computing $\tilde{\psi}_{in,d}$, but not an order of h .

2.5.4 Convergence Rates for Spatially Discretized 1-D Domains

Here, we consider a homogeneous pure absorber material placed in a 1-D slab configuration and uniformly mesh the domain using N_{cells} cells. We use: $x \in [0, 10 \text{ cm}]$,

$\sigma_t = 1 \text{ [cm}^{-1}\text{]}$, no external sources, vacuum conditions on the right face of the slab, and a normally incident unit beam on the left face. The analytical solution to this problem is trivial to obtain:

$$\psi(x, \mu_d) = \begin{cases} \exp[-\sigma_t x] & \mu_d = 1 \\ 0 & \text{otherwise} \end{cases}. \quad (2.41)$$

The L_2 norm of the error is:

$$E_\psi = \sqrt{\sum_{i=1}^{N_{cells}} \int_{x_{i-1/2}}^{x_{i+1/2}} \left(\psi(x, \mu_d) - \tilde{\psi}_{d,i}(x) \right)^2 dx}, \quad (2.42)$$

where we recall that $\tilde{\psi}_{d,i}(x)$ is the DFEM approximation of the angular flux in cell i . To evaluate the above integral, we use a high-order Gauss quadrature set $(x_{f,q}, w_{f,q})$ that employs a large number of quadrature points:

$$E_\psi \approx \sqrt{\sum_{i=1}^{N_{cells}} \frac{\Delta x_i}{2} \sum_{q=1}^{N_{gf}} w_{f,q} \left(\psi(x_{f,q}, \mu_d) - \tilde{\psi}_d(x_{f,q}) \right)^2}. \quad (2.43)$$

Values of E_ψ shown here are calculated using $N_{gf} = 10$. In addition to the L_2 error, we also present the cell average angular flux error, E_{ψ_A} , defined as

$$E_{\psi_A} = \sqrt{\sum_{i=1}^{N_{cells}} \Delta x_i \left(\psi_{A,d,i} - \tilde{\psi}_{A,d,i} \right)^2}, \quad (2.44)$$

and the cell outflow error, $E_{\psi_{out}}$, given by:

$$E_{\psi_{out}} = \sqrt{\sum_{i=1}^{N_{cells}} \Delta x_i \left(\psi(x_{i+1/2}, \mu_d) - \tilde{\psi}_{out,d,i} \right)^2}. \quad (2.45)$$

In Eq. (2.43), Eq. (2.44), and Eq. (2.45), Δx_i is the cell width of cell i and $\psi_{A,d,i}$ is the exact cell-averaged angular flux in cell i , which, for $\mu_d = 1$, is simply:

$$\psi_{A,d,i} = \exp[-\sigma_t x_{i-1/2}] \frac{1}{\Delta x_i} (1 - \exp[-\sigma_t \Delta x_i]) . \quad (2.46)$$

In the plots that follow, we omit plotting the errors of Exact DFEM since the Exact DFEM solution is identical to that of SL Gauss. For linear and quadratic polynomials, we plot only SL Lobatto and omit plotting TL and SL Newton-Cotes since these methods yield identical solutions for linear and quadratic trial spaces. Figures

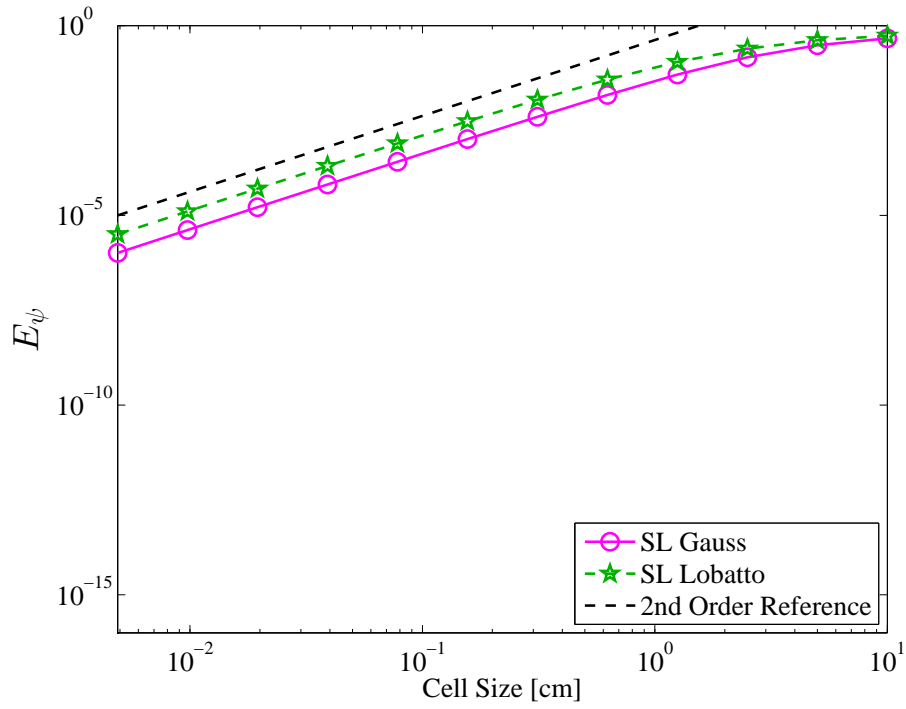


Figure 2.13: Convergence rate of the L_2 norm of the error, E_ψ , as a function of the mesh cell size for a pure absorber ($\sigma_t(x) = 1 \text{ [cm}^{-1}]$ and $x \in [0, 10 \text{ [cm]]}$).

2.13-2.16 mirror the results of Table 2.4, which is expected since the convergence

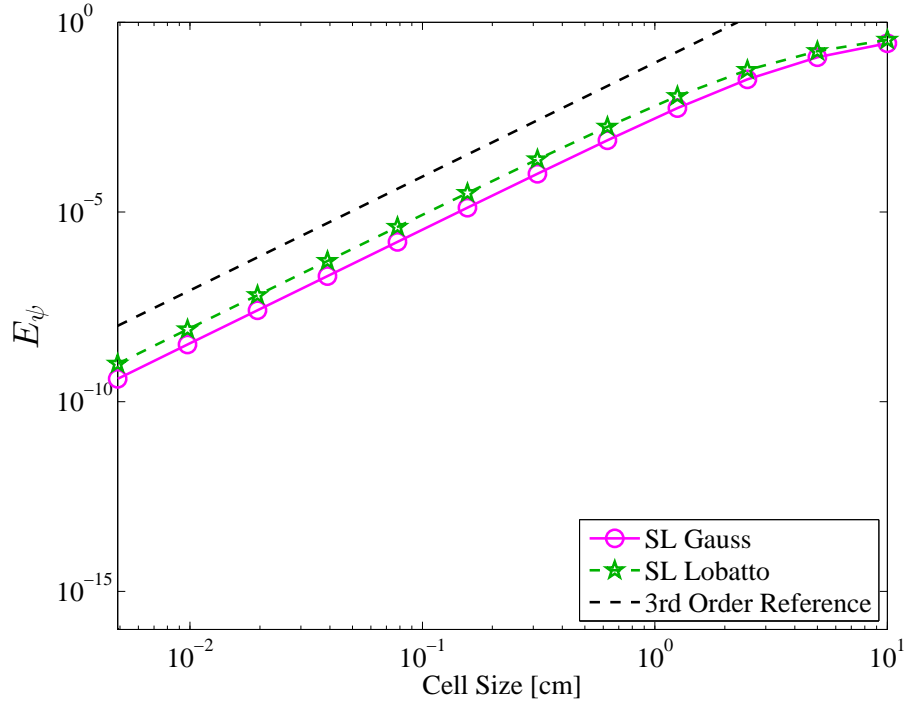


Figure 2.14: Convergence rate of the L_2 norm of the error, E_ψ , as a function of the mesh cell size for a pure absorber ($\sigma_t(x) = 1$ [cm⁻¹] and $x \in [0, 10$ [cm]]).

rate of E_ψ will be limited by the slowest converging local approximation which is $\tilde{\psi}_{in,d}$. Similarly, Figs. 2.17-2.20 are the multiple-cell analogue of the local truncation error analysis of $\tilde{\psi}_{A,d}$ given in Table 2.5. $E_{\psi_{out}}$, as shown in Figs. 2.21-2.24, does not converge at the local truncation error rates of Table 2.6. The accumulation of errors in multiple-cell problems causes $E_{\psi_{out}}$ to globally converge one order of accuracy lower than the local truncation orders given in Table 2.6. It should be noted that the plateauing of errors E_ψ , E_{ψ_A} , and $E_{\psi_{out}}$ to values $\approx 10^{-14}$ in Figs. 2.13-2.16, Figs. 2.17-2.20, and Figs. 2.21-2.24, respectively, is simply a result of our numerical solutions being limited by machine precision (double precision).

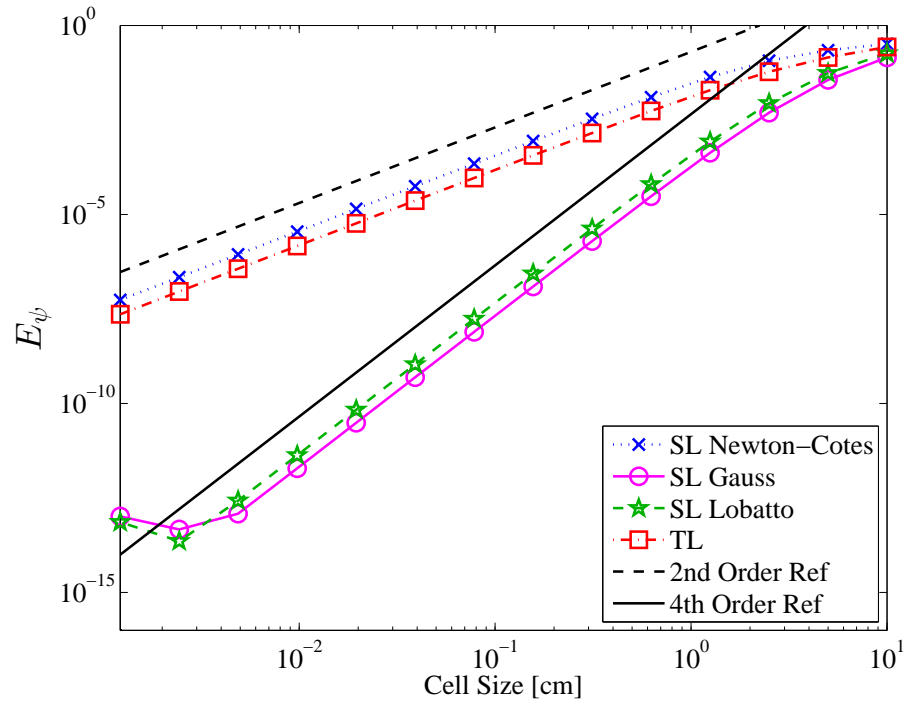


Figure 2.15: Convergence rate of the L_2 norm of the error, E_ψ , as a function of the mesh cell size for a pure absorber ($\sigma_t(x) = 1 \text{ [cm}^{-1}]$ and $x \in [0, 10 \text{ [cm]]}$).

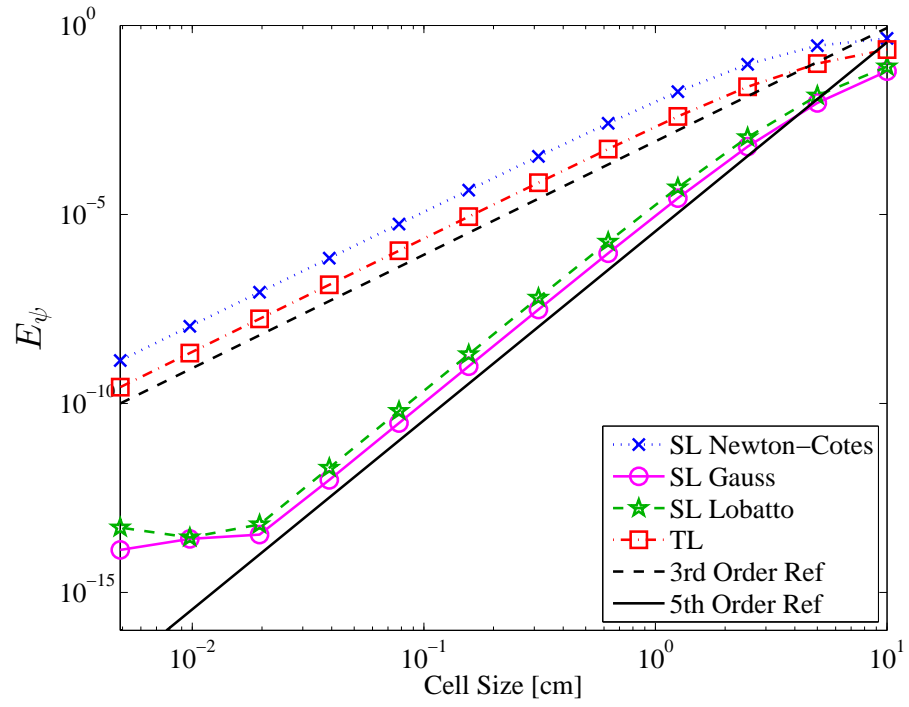


Figure 2.16: Convergence rate of the L_2 norm of the error, E_ψ , as a function of the mesh cell size for a pure absorber ($\sigma_t(x) = 1 \text{ [cm}^{-1}]$ and $x \in [0, 10 \text{ [cm]]}$).

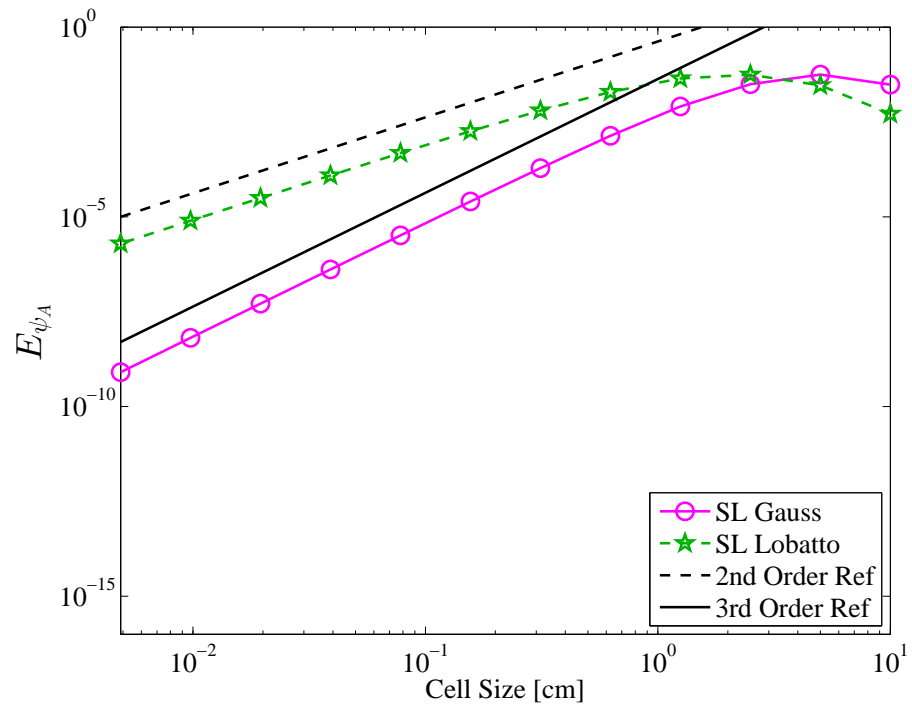


Figure 2.17: Convergence rate for $E_{\psi,A}$ as a function of the mesh cell size for a homogeneous pure absorber and linear DFEM.

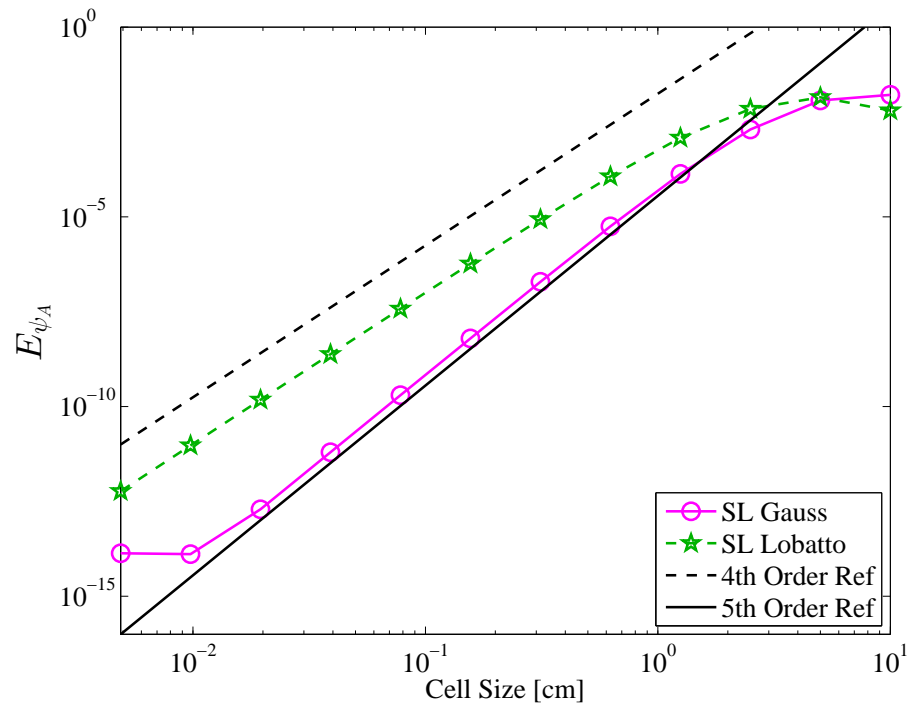


Figure 2.18: Convergence rate for $E_{\psi,A}$ as a function of the mesh cell size for a homogeneous pure absorber and quadratic DFEM.

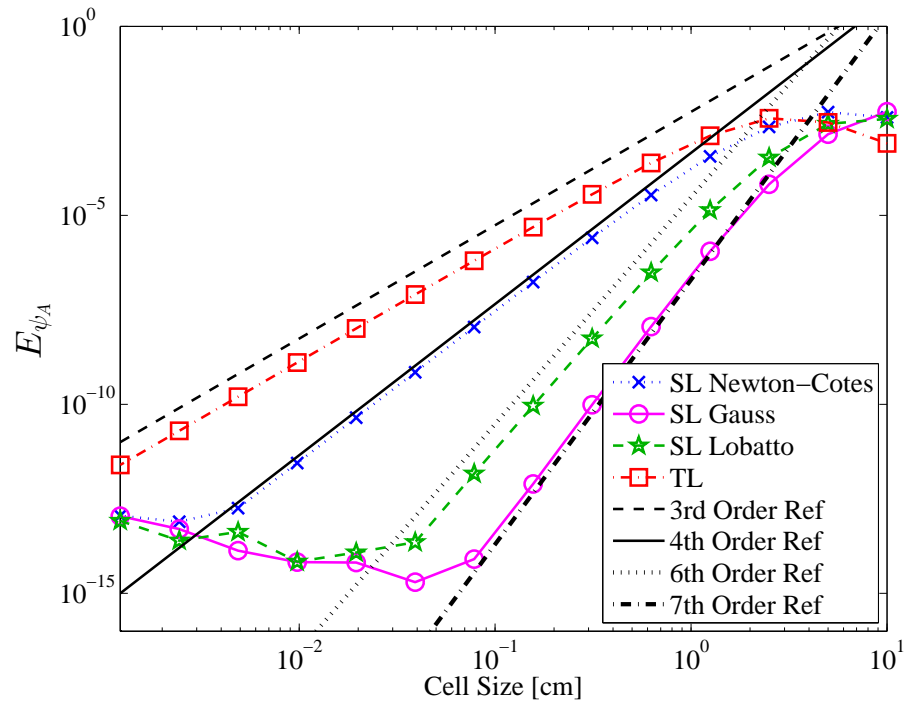


Figure 2.19: Convergence rate for $E_{\psi,A}$ as a function of the mesh cell size for a homogeneous pure absorber and cubic DFEM.

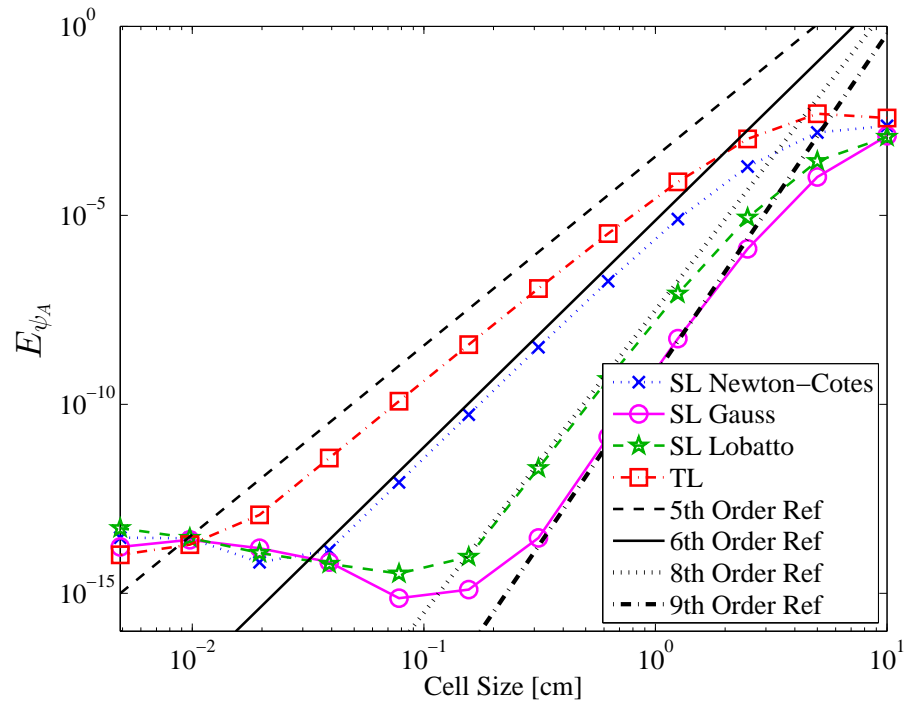


Figure 2.20: Convergence rate for $E_{\psi,A}$ as a function of the mesh cell size for a homogeneous pure absorber and quartic DFEM.

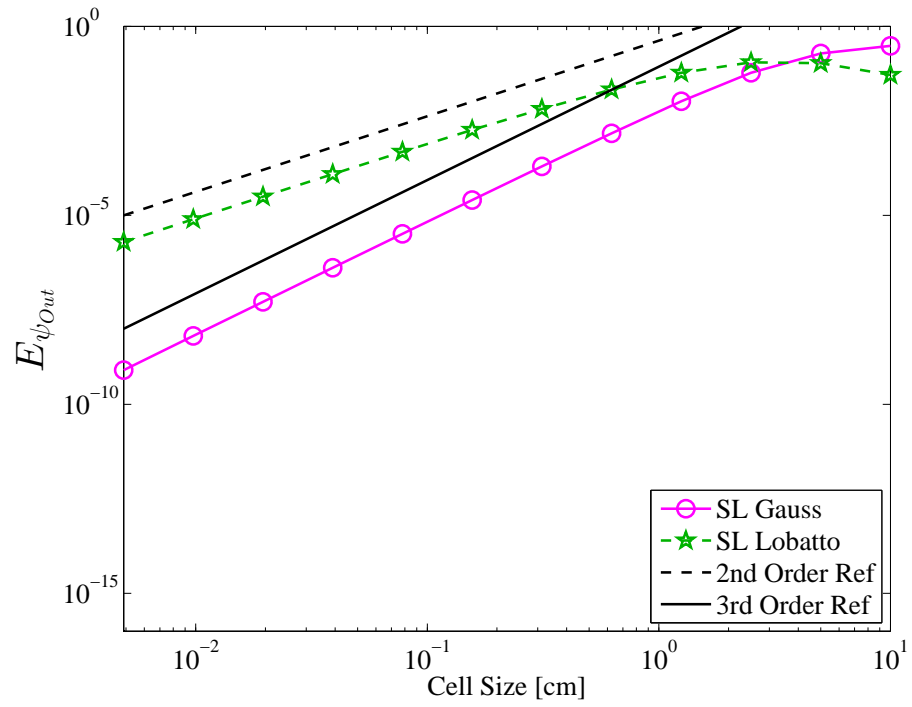


Figure 2.21: Convergence rate of $E_{\psi, out}$ as a function of the mesh cell size for a homogeneous pure absorber for linear DFEM.

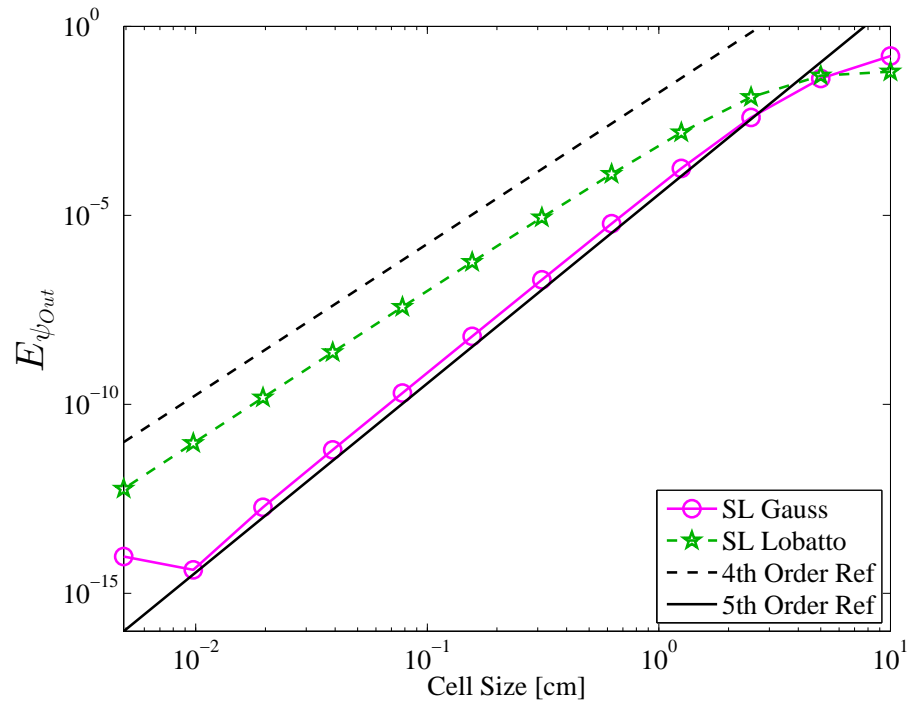


Figure 2.22: Convergence rate of $E_{\psi, out}$ as a function of the mesh cell size for a homogeneous pure absorber for quadratic DFEM.

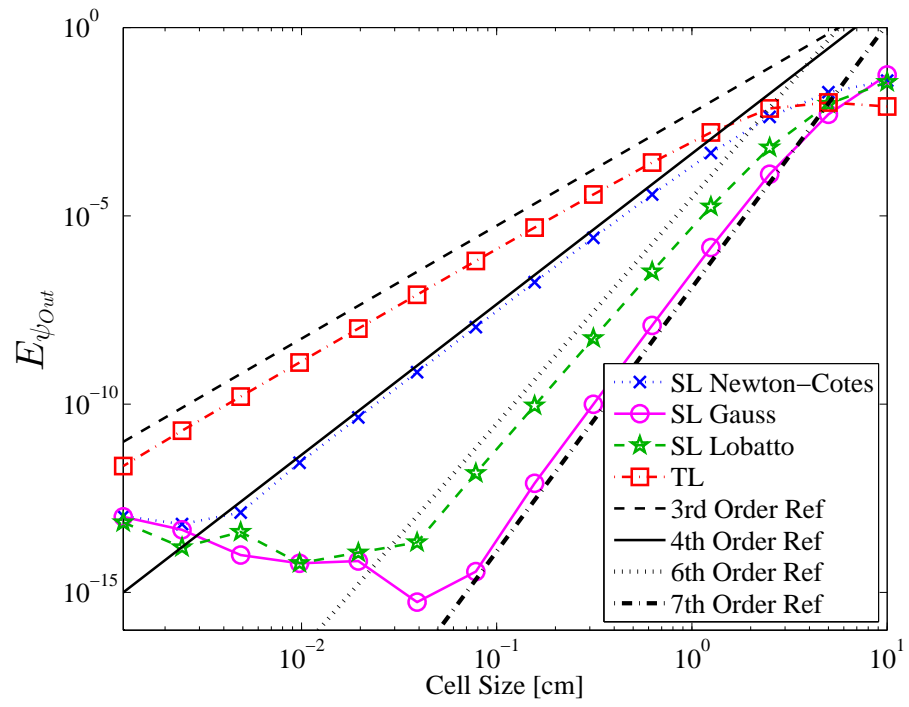


Figure 2.23: Convergence rate of $E_{\psi, out}$ as a function of the mesh cell size for a homogeneous pure absorber for cubic DFEM.

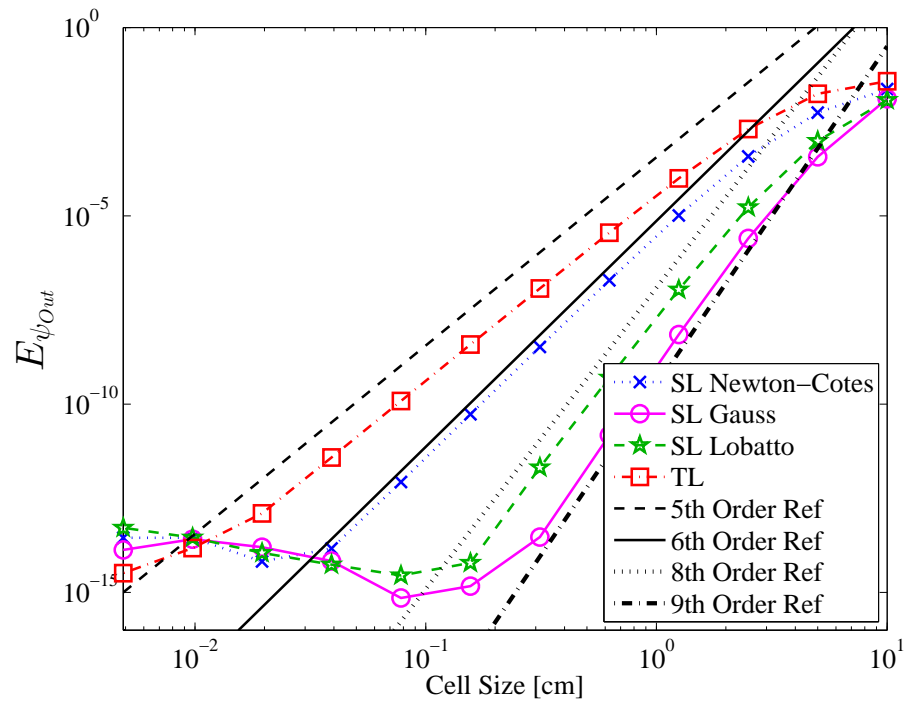


Figure 2.24: Convergence rate of $E_{\psi, out}$ as a function of the mesh cell size for a pure absorber for quartic DFEM.

3. LAST CHAPTER: THE IMPORTANCE OF RESEARCH

Thermal radiative transfer interaction opacities can be rapidly varying functions of temperature. For example, consider Marshak wave problems and the canonical T^{-3} dependence [19] of absorption opacity. Opacity variations of several orders of magnitude near the heated/cold material interface are easily possible. Historically, the neutron transport and thermal radiative transfer communities assumed interaction cross section and opacities, respectively, were cell-wise constant [3, 14, 17]. Adams first described [2] and then presented computational results [4] for a “simple” corner balance (SCB) spatial discretization method that explicitly accounted for the spatial variation of opacity within individual spatial cells. The SCB scheme (which can be shown to be related to a LDFEM for certain geometries) accounts for opacity spatial variation within each cell via vertex-based quadrature evaluation. Similar strategies have been adapted to LDFEM radiative diffusion [19] and LDFEM TRT [18] calculations. For accurate TRT solutions, use of higher order DFEM will require the development of corresponding higher order strategies for treating the within cell spatial variation of opacities.

3.1 New Section

3.2 Another Section

Text between the figures. Text between the figures. Text between the figures.
Text between the figures. Text between the figures. Text between the figures. Text
between the figures. Text between the figures. Text between the figures. Text
between the figures. Text between the figures. Text between the figures.

3.2.1 Subsection

3.2.2 Subsection

A table example is going to follow.

3.2.2.1 This is a subsubsection

3.3 Another Section



Figure 3.1: TAMU figure

Table 3.1: This is a table template

Product	1	2	3	4	5
Price	124.-	136.-	85.-	156.-	23.-
Guarantee [years]	1	2	-	3	1
Rating	89%	84%	51%		45%
Recommended	yes	yes	no	no	no

4. LAST CHAPTER: THE IMPORTANCE OF RESEARCH

4.1 New Section

5. LAST CHAPTER: THE IMPORTANCE OF RESEARCH

5.1 New Section

6. LAST CHAPTER: THE IMPORTANCE OF RESEARCH

6.1 New Section

fix spacing in bibliography, if any...

REFERENCES

- [1] M. Abramowitz and I. A. Stegun. *Handbook of Mathematical Functions with Formulas, Graphs, and Mathematical Tables*. United States Department of Commerce, Washington, D.C., 1972.
- [2] M. L. Adams. Subcell balance methods for radiative transfer on arbitrary grids. *Transport Theory and Statistical Physics*, 26(4 & 5):385–431, 1997.
- [3] M. L. Adams. Discontinuous finite element transport solutions in thick diffusive problems. *Nuclear Science and Engineering*, 137:298–333, 2001.
- [4] M. L. Adams and P. F. Nowak. Asymptotic analysis of a computational method for time- and frequency- dependent radiative transfer. *Journal of Computational Physics*, 46:366–403, 1998.
- [5] R. Alexander. Diagonally implicit runge-kutta methods for stiff o.d.e.’s. *SIAM Journal of Numerical Analysis*, 14(6):1006–1021, 1977.
- [6] S. Hamilton and M. Benzi and J. S. Warsa. Negative flux fixups in discontinuous finite elements in transport. In *International Conference on Mathematics, Computational Methods & Reactor Physics*, Saratoga Springs, New York, May 2009.
- [7] Y. Azmy. Arbitrarily high order characteristic methods for solving the neutron transport equation. *Annals of Nuclear Energy*, 19(7):593–606, 1992.
- [8] J. P. Hennart and E. del Valle. A generalized nodal finite element formalism for discrete ordinate equations in slab geometry: Part ii theory in the discontinuous moment case. *Transport Theory and Statistical Physics*, 24:479–504, 1995.

- [9] J. P. Hennart and E. del Valle. A generalize nodal finite element formalism for discrete ordinate equations in slab geometry: Part iii numerical results. *Transport Theory and Statistical Physics*, 24:505–533, 1995.
- [10] E. W. Larsen and W. F. Miller. Convergence rates of spatial difference equations for the discrete-ordinates neutron transport equations in slab geometry. *Nuclear Science and Engineering*, 73:76–83, 1980.
- [11] E. W. Larsen and J. E. Morel. Asymptotic solutions of numerical transport problems in optically thick, diffusive regimes ii. *Journal of Computational Physics*, 83:212–236, 1989.
- [12] E. W. Larsen and P. Nelson. Finite-difference approximations and superconvergence for the discrete ordinates equations in slab geometry. *SIAM Journal of Numerical Analysis*, 19(2):334–348, 198.
- [13] K. D. Lathrop. Spatial differencing of the transport equation: Positivity vs. accuracy. *Journal of Computational Physics*, 4:475–498, 1969.
- [14] E. E. Lewis and W. F. Miller. *Computational Methods of Neutron Transport*. American Nuclear Society, La Grange Park, IL, 1993.
- [15] P. G. Maginot, J. E. Morel, and J. C. Ragusa. A non-negative moment preserving spatial discretization scheme for the linearized boltzmann transport equation in 1-d and 2-d cartesian geometries. *Journal of Computational Physics*, 231(20):6801–6826, 2012.
- [16] The MathWorks. Matlab 2011b, 2011.
- [17] J. E. Morel, T. A. Wareing, and K. Smith. A linear-discontinuous spatial differencing scheme for s_n radiative transfer calculations. *Journal of Computational Physics*, 128:445–462, 1996.

- [18] J. E. Morel, T.-Y. B. Yang, and J. S. Warsa. Linear multifrequency-grey acceleration recast for preconditioned krylov iterations. *Journal of Computational Physics*, 227:244–264, 2007.
- [19] C. C. Ober and J. N. Shadid. Studies on the accuracy of time-integration methods for the radiation-diffusion equations. *Journal of Computational Physics*, 195:743–772, 2004.
- [20] P. A. Raviart. The use of numerical integration in finite element methods for solving parabolic equations. In *Conference on Numerical Analysis, RIANA 1972*, pages 233–264, August 1972.
- [21] W. H. Reed, T. R. Hill, F. W. Brinkley, and K. D. Lathrop. Triplet: A two-dimensional, multigroup, triangular mesh, planar geometry, explicit transport code. Technical Report LA-5428-MS, Los Alamos Scientific Lab, 1973.
- [22] K. Salari and P. Knupp. Code verification by the method of manufactured solutions. Technical Report SAND2000-1444, Sandia National Labs, 2000.
- [23] B. Su and G. L. Olson. An analytical benchmark for non-equilibrium radiative transfer in an isotropically scattering medium. *Annals of Nuclear Energy*, 24(13):1035–1055, 1997.
- [24] V. Thomee. *Galerkin Finite Element Methods for Parabolic Problems*. Springer, New York, 1997.
- [25] W. F. Walters. The relation between finite element methods and nodal methods in transport theory. *Progress in Nuclear Energy*, 18:21–26, 1986.
- [26] Y. Wang and J. C. Ragusa. A high-order discontinuous galerkin method for the sn transport equations on 2d unstructured triangular meshes. *Annals of Nuclear Energy*, 36(7):931–939, 2009.

- [27] Y. Wang and J. C. Ragusa. On the convergence of dgfem applied to the discrete ordinates transport equation for structured and unstructured triangular meshes. *Nuclear Science and Engineering*, 163:56–72, 2009.
- [28] J. S. Warsa and A. K. Prinja. p-adaptive numerical methods for particle transport. *Transport Theory and Statistical Physics*, 28(3):229–270, 1999.

APPENDIX A

FIRST APPENDIX

Text for the Appendix follows.



Figure A.1: TAMU figure

APPENDIX B

SECOND APPENDIX WITH A LONGER TITLE - MUCH LONGER IN FACT

Text for the Appendix follows.

B.1 Appendix Section



Figure B.1: TAMU figure